A Study of Polarization in Hyperon Production Processes

A THESIS

SUBMITTED TO THE FACULTY OF THE GRADUATE SCHOOL

OF THE UNIVERSITY OF MINNESOTA

BY

David McDill Woods

IN PARTIAL FULFILLMENT OF THE REQUIREMENTS

FOR THE DEGREE OF

DOCTOR OF PHILOSOPHY

January, 1995

A Study of Polarization in Hyperon Production Processes

by David McDill Woods

Under the supervision of Professor Kenneth J. Heller

ABSTRACT

The polarization of Ξ^- and Ω^- hyperons produced from both polarized and unpolarized neutral particle beams has been studied. The unpolarized neutral beam production studies are the first measurements made using this production technique. The neutral beam consisted of neutrons, Λ^0s, Ξ^0s, K^0s, and photons. No polarization was observed in the sample of 1.4×10^7 Ξ^-s produced by an unpolarized neutral beam. For Ω^-s produced by an unpolarized neutral beam, a sample of 1.7×10^5 events with an average momentum of 394. GeV/c had a polarization of $+0.044\pm0.008$ and a sample of 5×10^4 events with an average momentum of 304. GeV/c had a polarization of $+0.036\pm0.015$. The polarization of 7.1×10^5 Ξ^-s produced by a polarized neutral beam was -0.118 ± 0.004 at an average momentum of 393. GeV/c. 1.8×10^4 Ω^-s produced by the polarized neutral beam had a polarization of -0.069 ± 0.023 at an average momentum of 394. GeV/c. The measurements for production from a polarized neutral beam are in agreement with a previous measurement.

Acknowledgements

My fellow graduate students in the University of Minnesota High Energy Physics group deserve thanks for their patience when I was using most of the available CPU time on this computer system. The entire Fermilab staff deserves credit for their assistance in setting up and running the experiment.

In addition to the people who provided technical and scientific assistance to me during my time in graduate school, I benefitted greatly from personal relationships with many people. First and foremost are my family, who have supported and encouraged me throughout my life. They also provided the genes(see references 1 and 2), which seem to have helped. Thanks to my father and grandfather, who inspired me and showed me what fun physics could be from an early age. My sister Ann, who lived in the same city as me through much of my time in graduate school, deserves special credit for putting up with me for so long.

Thanks to Jerry and Noah for making work fun and not working even more fun. Eileen deserves thanks for being a most excellent source of suggestions of fun and interesting things to do. Ken Johns shared many late night shifts with me and made them fun and productive. Pete provided interesting music to listen to and fun toys to play with during shifts, and also told us when it was time to go to lunch. Dave Ciampa provided advice about how life and the world really work. Graham Allan was always ready to offer witty commentary on life in the physics department. Thanks also to Alex Ayala-Mercado, John Capriotti, Dave Fein, Milena Groblewski-Higgins, Eric James, Krista Mullman, and Tricia Tynan for their contributions. Thanks also to all the people I'm sure I've neglected to mention.

Thanks also to Bill Watterson and Universal Press Syndicate for granting me permission to reprint the Calvin and Hobbes cartoons in my thesis, and also for providing a constant source of amusement.

CALVIN AND HOBBES copyright Watterson. Dist. by UNIVERSAL PRESS SYNDICATE. Reprinted with permission. All rights reserved.

Dedication

This dissertation is dedicated to my father and grandfather, who inspired me and showed me what fun science could be.

Table of Contents

List of Tables

List of Figures

xiv

Chapter 1

Introduction

For many years, physicists have studied the interaction of particles to understand the basic forces of nature. These investigations have progressed to higher energies as the particles being studied have become smaller. In the early part of this century, atomic spectra were studied to understand the interaction between electrons and nuclei in atoms[1]. Later came the study of nuclear spectra to understand the structure of the nucleus[2]. Now, we study quarks and leptons to understand the fundamental forces of nature. The purpose of this experiment was to learn about quark interactions by studying the production of polarized hyperons.

1.1 Hyperon Polarization

Hyperon polarization in inclusive proton production reactions was first observed in a Λ^0 production experiment at Fermilab in 1976[3]. Since then, extensive experimental and theoretical efforts have been made in an attempt to explain this phenomena. Despite these efforts, a simple, concise explanation of the cause of polarization in hyperon
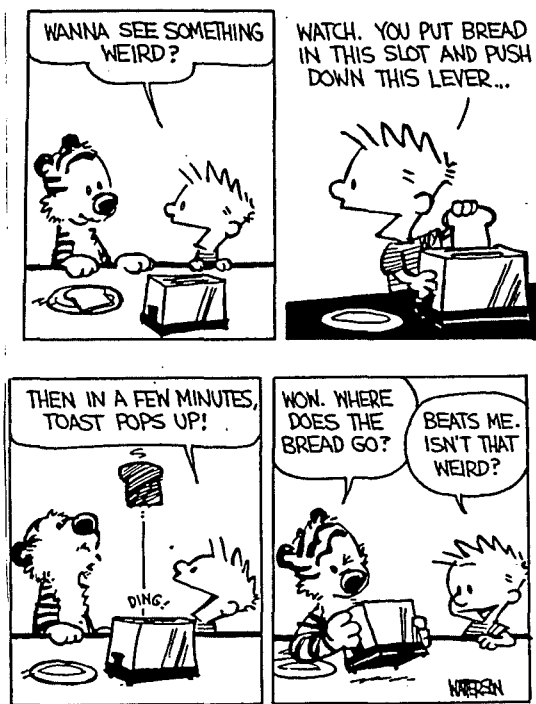
production has not been found. In addition to the Λ^0, high energy polarization measurements have been made on many other baryons produced in proton interactions, including the proton, $\overline{\Lambda}$, Σ^+, Σ^0, Σ^-, $\overline{\Sigma}^-$, Ξ^-, Ξ^0, $\overline{\Xi}^+$, and Ω^- [4, 5, 6, 7, 8, 9, 10, 11, 12, 13]. These polarization measurements are a sensitive way of studying quark interactions since they reflect the interference between the spin dependent and spin independent parts of the production process. There are many different ways of studying polarization phenomena, including production by polarized and unpolarized incident beams. The fact that the observed effects are large indicates that spin contributions are an important part of the strong interaction.

The technique used by most previous experiments to produce polarized samples is shown in Figure 1.1. In this method, a beam of unpolarized particles strikes a target from a known direction. In Figure 1.1, $\hat{i}$ is the direction of the incident beam, $\hat{j}$ is the direction of the produced particle, and θ is the production angle. The only parity conserving direction in this interaction is perpendicular to the production plane defined by $\hat{i} \times \hat{j}$. Since spin is invariant under a parity transformation, and the strong force that governs this interaction conserves parity, the spin of the produced particles must be perpendicular to the production plane.

Experiments have also been conducted using incident π, Λ, K, and ν, and γ beams[14, 15, 16, 17, 18]. There have been other experiments that have used polarized proton beams to study spin transfer process[19, 20, 21]. In addition, Λ polarization has been observed in a pp collider experiment[22]

One experiment has used the proton production technique to produce a secondary polarized neutral beam which was then used to produce a tertiary negatively charged beam. This experiment studied how the polarization of the secondary beam was transferred to the tertiary beam. This technique was used to produce polarized samples of Ω^- hyperons that were not polarized when produced directly from protons[13].
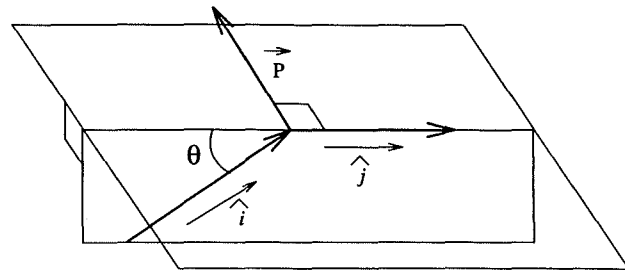
Figure 1.1: Production of a polarized hyperon sample from an incident proton beam.

1.2 Previous Polarization Results

Any inclusive reaction can be characterized by three kinematic variables: beam energy, transverse momentum (p_T), and longitudinal momentum or Feynman x (x_F). These quantities are given by:

$$p_T = p\sin\theta \tag{1.1}$$

$$x_F = \frac{p_l{}^*}{p_{l\ max}{}^*} \tag{1.2}$$

where θ is the production angle, p is the momentum of the particle produced in the interaction, $p_l{}^*$ is the longitudinal momentum of the produced particle in the center of mass frame, and $p_{l\ max}{}^*$ is the maximum longitudinal momentum. For the results presented here, where the produced particle is in the forward direction, and the energy is much greater than the mass, x_F can be approximated by

$$x_F = \frac{P_{produced}}{P_{beam}} \tag{1.3}$$

where $P_{produced}$ and P_{beam} are the laboratory frame momenta of the produced hyperon and the incident beam respectively.

Figure 1.2 shows previous polarization results as a function of momentum for 400 GeV protons producing Λs, $\overline{\Lambda}$s, Σ^-s, Ξ^0s, and Ξ^-s at a production angle of 7.5 mrad[5, 7, 10, 11, 23]. Note that the sign of the polarization of the Λs, Ξ^0s, and Ξ^-s is opposite
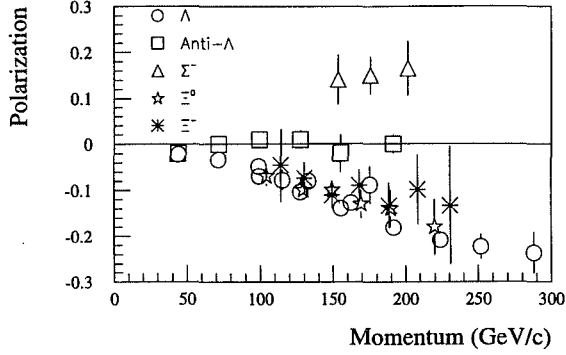
Figure 1.2: Polarization as a function of momentum at 400GeV incident beam energy.

Figure 1.3: Polarization as a function of p_T at 400 GeV incident beam energy.

the sign of the polarization of the Σ^-s, and that the $\overline{\Lambda}$s are unpolarized. Data at other production angles show that Σ^+s and Σ^0s are polarized with the same sign as the Σ^-s [6, 8] .

Figures 1.3 and 1.4 show these same polarization results as a function of p_T and as a function of x_F [5, 7, 10, 23]. Λ^0 polarization has been studied at a variety of energies and no significant energy dependence has been found. In addition, studies of Λ^0 production from a variety of different nuclear targets show no variation [23]. Similar studies for the polarization of proton produced Ξ^0s show no target dependence [11].

A more recent experiment made a detailed study of polarization for Ξ^-s [24]. These results show that P_{Ξ^-} and P_Λ have similar behavior as a function of p_T, but their x_F behavior is different. In addition, comparison of these results, which were obtained with 800 GeV incident protons, to 400 GeV data with similar p_T and x_F, showed that unlike P_Λ, P_{Ξ^-} does depend on the incident beam energy.

Figure 1.4: Polarization as a function of x_F at 400GeV incident beam energy.
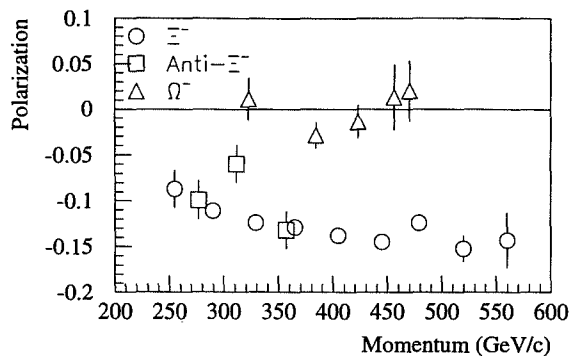
Figure 1.5: Polarization as a function of momentum at 800 GeV incident beam energy.

This same experiment also studied the polarization of Ω^-s, and $\overline{\Xi}^+$s produced using an 800 GeV incident proton beam[12, 13, 24]. A comparison of Ξ^-, Ω^-, and $\overline{\Xi}^+$ polarization at a production angle of 2.5 mrad are shown in Figure 1.5. This was the first experiment to observe anti-hyperon polarization. In addition, it can be seen that Ω^-s produced from protons are not polarized. This is the first hyperon where polarization has not been observed in proton production. Another recent result has shown that $\overline{\Sigma}^-$s produced from protons are also polarized[9].

Since Ω^-s produced by a proton beam were observed to be unpolarized, another method was used to make polarized Ω^-. In this method, referred to as spin transfer production, the proton beam was used to produce a neutral beam containing neutrons, γs, K^0s, Λs and Ξ^0s. The proton beam struck a target at a non-zero production angle, producing polarized Λs and Ξ^0s in the neutral beam. This neutral beam, which was basically a beam of polarized strange quarks, was then used to produce a sample of Ξ^-s
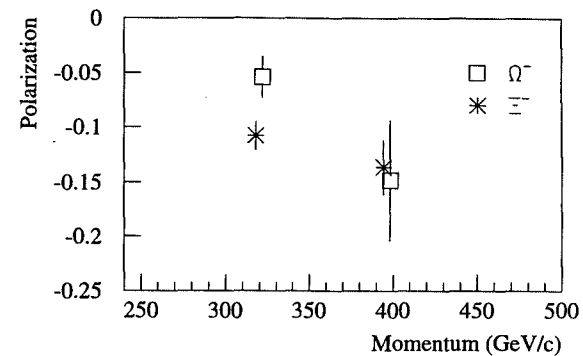
Figure 1.6: Polarization results for the spin transfer method at 800 GeV.

and Ω^-s, with the expectation that the polarized strange quarks would be transferred to the Ξ^-s and Ω^-s. The results for this production method are shown in Figure 1.6. These results show that both the Ξ^- s and Ω^-s produced by this method are polarized [25, 26]. This spin transfer method was also studied by an earlier experiment that observed the transfer of polarization from a polarized proton beam to Λs and Σ^0s[21].

1.3   Polarization Theory

There are several models that attempt to explain the observed polarization phenomena. Most of these models use quark ideas and assume that the hyperon is formed from a fragment of the incident particle and one or more quarks from the quark sea. For instance, Ξ^- (dss) production from protons can be seen as the d quark from the incident proton combining with two s quarks from the sea.

Perturbative quantum chromodynamics (pQCD) has been used to calculate the transverse polarization of produced quarks with the result that

$$P \propto \frac{m}{p_T^2} \qquad (1.4)$$

where m is the quark mass, and p_T is the transverse momentum[27]. However, this is a perturbative calculation that can only be applied to problems where the energy scale of the problem is much larger than Λ_{QCD}, which has a value in the range 0.1 to 0.5 GeV [28]. Equation 1.4 predicts that the polarization should be zero at high transverse momentum. The highest p_T value reached in polarization measurements is a study of Λ^0 polarization in a region up to 3.8 GeV/c [23], a region where the pQCD prediction is only marginally applicable. However, in the experimental measurements, there is no indication that the polarization is tending towards zero.

At the opposite end of the energy spectrum from the pQCD calculation is a naive quark model polarization theory, constructed using only the simple spin/flavor SU(6) wave functions for the baryons given in Table 1.1. Construction of this model was encouraged by the reasonable agreement between hyperon magnetic moments calculated using the simple quark model and experimental observations. The wave functions provide a simple explanation for the most striking property of hyperon polarization, namely the different signs of the measured polarizations. If it is assumed that the strong production mechanism always polarizes the s quark in the same direction, the wave functions show that Σ^+s, Σ^0s, and Σ^-s should have polarizations opposite to those of Λs, Ξ^-s, Ξ^0s, and Ω^-s. If the proton beam is unpolarized, then the u and d quarks from the incident proton that are retained in the final state should have no preferred spin direction. From Table 1.1, it can be seen that for the spin $\frac{1}{2}$ strange hyperons, the wave functions can be seen as either a combination of a spin 1 ud diquark and a single s quark or a combination of a spin 1 ss diquark with a single u or d quark. In either case, if only one direction is allowed for the s quark spin, a direct correlation between

Baryon	Quark wave function
$p \uparrow$	$\sqrt{2/3}u \uparrow u \uparrow d \downarrow - \sqrt{1/6}\,(u \uparrow u \downarrow + u \downarrow u \uparrow)d \uparrow$
$n \uparrow$	$\sqrt{2/3}d \uparrow d \uparrow u \downarrow - \sqrt{1/6}\,(d \uparrow d \downarrow + d \downarrow d \uparrow)u \uparrow$
$\Lambda \uparrow$	$\sqrt{1/2}(u \uparrow d \downarrow - u \downarrow d \uparrow)s \uparrow$
$\Sigma^+ \uparrow$	$\sqrt{2/3}u \uparrow u \uparrow s \downarrow - \sqrt{1/6}\,(u \uparrow u \downarrow + u \downarrow u \uparrow)s \uparrow$
$\Sigma^0 \uparrow$	$\sqrt{2/3}u \uparrow d \uparrow s \downarrow - \sqrt{1/6}\,(u \uparrow d \downarrow + u \downarrow d \uparrow)s \uparrow$
$\Sigma^- \uparrow$	$\sqrt{2/3}d \uparrow d \uparrow s \downarrow - \sqrt{1/6}\,(d \uparrow d \downarrow + d \downarrow d \uparrow)s \uparrow$
$\Xi^0 \uparrow$	$\sqrt{2/3}s \uparrow s \uparrow u \downarrow - \sqrt{1/6}\,(s \uparrow s \downarrow + s \downarrow s \uparrow)u \uparrow$
$\Xi^- \uparrow$	$\sqrt{2/3}s \uparrow s \uparrow d \downarrow - \sqrt{1/6}\,(s \uparrow s \downarrow + s \downarrow s \uparrow)d \uparrow$
$\Omega^- \uparrow$	$s \uparrow s \uparrow s \uparrow$

Table 1.1: The baryon SU(6) spin/flavor wave functions.

the s quark spin and the overall hyperon spin can be seen. In the Σ wave functions, there are both spin up and spin down s quark terms, however, the $s \downarrow$ term is larger. In the other hyperon wave functions, the $s \uparrow$ terms dominate.

One model hypothesizes that the final state polarization comes about during the recombination of the incident fragment and sea quarks to produce the final state. Other models account for the polarization by proposing methods by which the quarks produced from the sea have a preferred spin direction.

The most extensive model to date is that of DeGrand and Miettinen[29], who propose that the polarization is the result of a Thomas precession of the quark spins in the color field. The precession affects both the sea quarks and the quarks from the incident particle. This model also attempts to explain the transverse momentum (p_T) and Feynman x (x_F) dependence observed in studies of Λ polarization.

The latest version of this model also makes predictions for hyperons produced from polarized incident beams and for production from particles other than protons[30]. Table 1.2 lists these predictions as a function of d, ϵ, ϵ', δ and δ'. Here d is the incident beam polarization, ϵ and δ are the polarization contributions of the single quark and diquark respectively for processes where the diquark comes from the incident particle, and ϵ' and δ' are the single quark and diquark contributions for processes where the

Interaction	Polarization
$p \leftrightarrow \Lambda^0, n \leftrightarrow \Lambda^0$	$-\epsilon$
$p \leftrightarrow \Sigma^+, n \leftrightarrow \Sigma^-, p \leftrightarrow \Sigma^0$ $n \leftrightarrow \Sigma^0, \Xi^0 \leftrightarrow \Xi^-$	$\frac{\epsilon + 2\delta + 2d}{3 + (2\epsilon + 2\delta)d}$
$p \leftrightarrow n, \Sigma^+ \leftrightarrow \Xi^0, \Sigma^- \leftrightarrow \Xi^-$ $\Sigma^\pm \leftrightarrow \Sigma^0, \Xi^0 \leftrightarrow \Sigma^0$	$\frac{-40\epsilon + \delta + d}{42 + (\epsilon + \delta)d}$
$\Sigma^\pm \leftrightarrow \Lambda^0, \Xi^0 \leftrightarrow \Lambda^0$ $\Xi^- \leftrightarrow \Lambda^0$	$\frac{-4\epsilon + \delta + d}{6 + (\epsilon + \delta)d}$
$p \to \Sigma^-, n \to \Sigma^+, \Sigma^+ \to \Xi^-$ $\Sigma^- \to \Xi^0, \Xi^0 \to p, \Xi^- \to n$	$\frac{12\epsilon' - 3\delta' - 4d}{18 + (-6\epsilon' - \delta')d}$
$p \leftrightarrow \Xi^-, n \leftrightarrow \Xi^0, \Sigma^+ \leftrightarrow \Sigma^-$	$\frac{-3\epsilon' - 6\delta' + d}{9 + (-3\epsilon' - 2\delta')d}$
$p \to \Xi^0, \Xi^0 \to \Sigma^-, \Sigma^- \to p$ $n \to \Xi^-, \Xi^- \to \Sigma^+, \Sigma^+ \to n$	$\frac{-3\epsilon' - 6\delta' - 2d}{9 + (6\epsilon' + 4\delta')d}$
$\Sigma^- \to \Omega^-$	$-\frac{5}{18}d + \frac{5}{6}(\epsilon - \delta)$
$\Xi^0, \Xi^- \to \Omega^-$	$\frac{5}{6}(\delta - \epsilon + d)$
$\Lambda^0 \to \Omega^-$	$\frac{5}{6}(\epsilon - \delta + d)$

Table 1.2: Polarization predictions of the model by DeGrand and Miettinen. ϵ, ϵ', δ, and δ' represent the polarization contribution of the single quark and diquarks and d is the incident polarization.

diquark originates in the sea. Initially, DeGrand and Miettinen did not differentiate between ϵ and ϵ' and δ and δ', but there is evidence that suggests that they are not equal[20, 31]. Experimental measurements require δ and ϵ to equal at the 20% level, with a value in the range 0.1 - 0.2.

Bonner et al.[21] have modified the DeGrand and Miettinen model to allow for spin flips in the fragment from the incident particle. It was observed that the measured Λ^0 to Σ^0 production ratio, which is spin dependent, was noticeably different from those

predicted by the DeGrand and Miettinen model [32]. The introduction of the spin flip terms was used to make predictions that were in closer agreement with the experimental observations. In this model there is some probability, $\mathcal{P}$, that the spin of a single quark will flip. This adds two parameters τ_1 and τ_2 to the model.

$$\tau_1 = \frac{\mathcal{P}}{1 - \mathcal{P}} \tag{1.5}$$

$$\tau_2 = \frac{2\mathcal{P}(1 - \mathcal{P})}{1 - 2\mathcal{P}(1 - \mathcal{P})} \tag{1.6}$$

τ_1 is the parameter for interactions where only one quark from the incident particle is present in the final state, and τ_2 is the parameter for cases when a diquark from the initial particle is present in the final state. Bonner et al. report a value of $\tau_2 = 0.38 \pm 0.04$ is needed to fit the observed ratio of the cross-sections for production of Σ^0s and Λ^0s from protons. This results in a spin flip probability, $\mathcal{P} \approx 0.16$, and a value of $\tau_1 \approx 0.19$. Table 1.3 gives predictions for hyperon polarization with the spin flip terms included for the interactions of interest to this experiment. A detailed example of these calculations is given in Appendix A. It should be possible to predict the expected final state polarization using the predictions given in Table 1.3. This will be discussed further in Chapter 6.

A model proposed by Andersson, Gustafson, and Ingelman[33], known as the Lund model, uses the production of $s\bar{s}$ pairs from the sea through a tunneling process to explain Λ polarization. This is a soft process where pQCD is not applicable. The tunneling process gives rise to an enhancement in the number of hyperons produced with their p_T in the same direction as the p_T of the s quark. In this process, the p_T of the s quark is related to its spin through the conservation of angular momentum. It is possible to extend the idea of this model to the production of anti-hyperons. If the idea of the production of a quark – anti-quark pair is extended to the production of a hyperon – anti-hyperon pair, it would predict that the sign of the polarization of

Interaction	Polarization
$n \to \Xi^-$	$\dfrac{2d(\tau_1-1)-(3\epsilon'+6\delta')(1+\tau_1)}{d(1-\tau_1)(6\epsilon'+4\delta')+9(1+\tau_1)}$
$\Lambda \to \Xi^-$	$\dfrac{d-4\epsilon+\delta(1+\tau_2)}{d(\epsilon+\delta)+6+2\tau_2}$
$\Xi^0 \to \Xi^-$	$\dfrac{2d+\epsilon+2\delta(1+\tau_2)}{2d(\delta+\epsilon)+3+4\tau_2}$
$n \to \Omega^-$	0
$\Lambda \to \Omega^-$	$\dfrac{5}{6}\dfrac{d+\epsilon'-\delta'+\tau_1(\epsilon'-\delta'-d)}{1+\tau_1}$
$\Xi^0 \to \Omega^-$	$\dfrac{10(d-\epsilon+\delta)+2\tau_2(5\delta-6\epsilon)}{10d\delta-8d\epsilon+12+14\tau_2}$

Table 1.3: Polarization predictions of the model by DeGrand and Miettinen with the addition of spin flip terms.

anti-hyperons produced in this manner should be opposite that of the hyperon. This does not match the experimental observations.

Szwed [34] has proposed a model for Λ polarization where the s quark polarization is due to multiple scattering of the s quark from the sea in the color field. This model also offers an explanation of the p_T dependence of the Λ and predicts no strong x_F dependence in this process.

A model proposed by Dharamaratna and Goldstein [35] explores the idea that the strange quark from the sea is produced by the fusion of two gluons. They conclude that s quarks produced by this process could be polarized, leading to the polarization of the produced Λ. They have calculated the dependence of Λ polarization on p_T and x_F, and these predictions agree with the experimental data. These calculations have not been extended to any other hyperons.

Barni et al. propose a model in which the final state Λ^0 can be produced by several processes including direct production, production from Σ^0 electromagnetic decays, and production from the decay of intermediate Σ^+ and Σ^* baryons [36]. In this model, the

final state polarization is due to interference between these various production channels. This model should also be applicable to Σ^+ and Σ^- production, however it is not clear that it can be extended to Ξ^0 and Ξ^- production.

A model proposed by Soffer [37] uses a pion exchange mechanism to explain Λ polarization. Once again, the final state Λ^0 can be produced from several intermediate states, and interference between these different production channels is used to explain the observed final state polarization. It successfully reproduces the observed p_T and x_F dependence of the Λ polarization. However, as with most of the other models, it has not been extended to any other processes.

While several models have been proposed to explain the observed hyperon polarization data, none of the models offers an acceptable explanation of all of the experimental data. The motivation of this experiment was to study hyperon polarization in a way that might offer further insight into the origin of this phenomena. To do this, Ξ^- and Ω^- hyperons were made using three different techniques. In addition to proton production, Ξ^-s and Ω^-s were made from both a polarized and an unpolarized neutral beam. The unpolarized neutral beam production was of special interest since the neutral beam would contain Λ^0s and Ξ^0s, and therefore, some of the strange quarks needed to produce the final state Ξ^-s and Ω^-s would already be present.
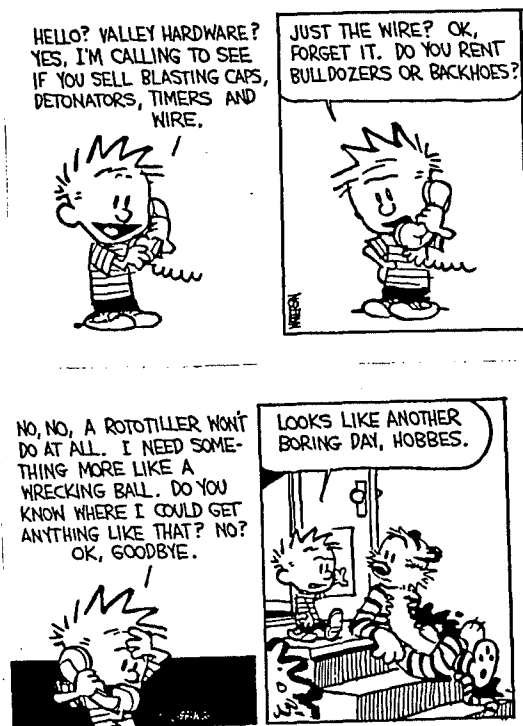
Chapter 2

Apparatus

The data used in this experiment were collected as part of Experiment 800 (E800) at Fermi National Accelerator Laboratory (Fermilab) located in Batavia, Illinois, a suburb of Chicago. E800 took data during a fixed target run that began in June 1991 and ended in January 1992. The beamline used to transport the incident protons to the target and make the hyperons that were to be studied, the spectrometer that detected the hyperons and their decay products, and the data acquisition system used to record the data were the most important parts of the experimental apparatus and are described here in detail.

2.1   The Beamline

The accelerator, called the TeVatron, produced a beam of approximately 10^{13} 800 GeV protons per spill. Each spill lasted 20 seconds with one spill per minute. The beamline used in this experiment was designed to transport a 800 GeV proton beam with an intensity of up to 2.5×10^{12} protons per spill.

The beamline contained dipole magnets used for horizontal and vertical beam positioning. It also had horizontal and vertical focusing quadrupole magnets. These
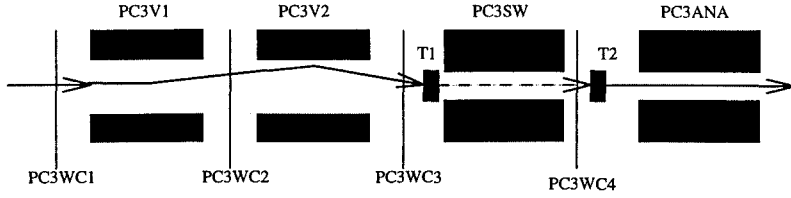
Figure 2.1: The downstream end of the beamline. This shows the beamline as it was configured for polarized neutral beam production.

magnets focused the beam so that it had a diameter of less than 2mm when it struck the target.

2.2 Targets and Sweeping Magnets

The different production modes used in this experiment required a high degree of flexibility in the downstream end of the beamline where the target stations were located. The downstream end of the beamline contained the magnets used to determine the angle at which the proton beam struck the upstream target. The production angles used were 0 mrad and ±1.8 mrad. The size of the production angle was mainly limited by the magnets available to bend the protons away from the centerline and then bring the beam back onto the target. The production angle was chosen to maximize the polarization and production rate, since as the production angle increased, the production rate decreased. Figure 2.1 is a schematic drawing of the downstream end of the beamline. The configuration of the beamline for the various production mode will be discussed in section 2.3. Dipole magnets PC3V1 and PC3V2 were used to control the production angle. Magnet PC3V1 was used to bend the protons up or down and magnet PC3V2 was used to bring the beam back onto the target.

PC3SW was a standard main ring B2 dipole magnet that was used to select a neutral beam. It had a field strength of 1.8 Tesla in the horizontal direction and was 6m long.
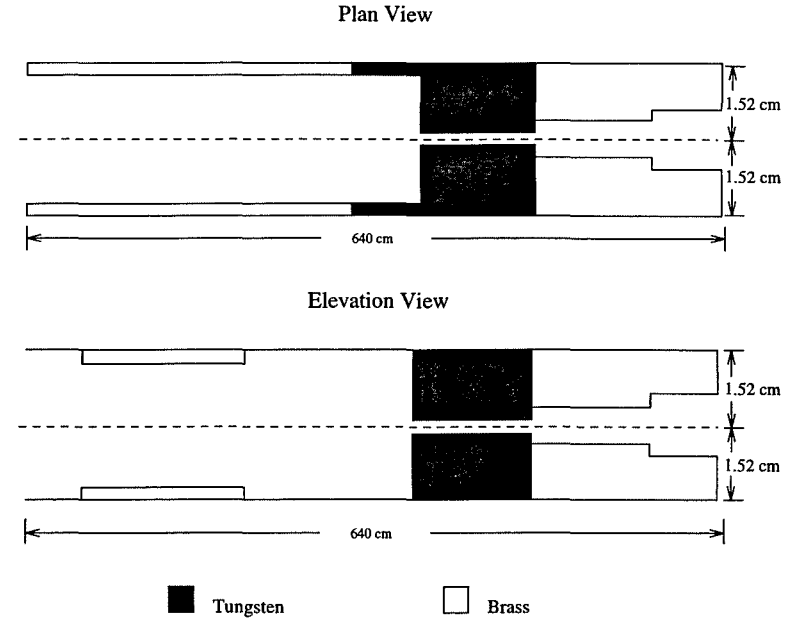
Figure 2.2: The neutral collimator in PC3SW.

The field direction was chosen to be in the horizontal direction to ensure that it would not precess the spin of the polarized particles that were transported through this magnet in one production mode. It was mounted on remotely controlled motorized jacks that allowed both ends of the magnet to be raised and lowered when the production angle was changed. Magnet PC3SW was used as both a proton beam dump and a neutral beam selector. Figure 2.2 shows the collimator inside magnet PC3SW. This collimator was made of brass and tungsten, with the tungsten segments placed where the proton beam was expected to dump when the incident angle was between 0.0 and 2.0 mrad. The defining aperture of the collimator was 0.25 cm by 0.25 cm.

Magnet PC3ANA, also referred to as the Hyperon magnet, was used to select a

negatively charged beam. Figure 2.3 shows the charged collimator in the Hyperon magnet. This collimator was designed with a central orbit momentum of 400 GeV at a magnetic field of 3.35 Tesla. Since this collimator was only designed to transport a tertiary beam of charged particles, it was constructed entirely of brass. The defining aperture of the collimator was 0.51 cm by 0.51 cm. This magnet also served to precess the spin of the particles passing through it, which was necessary for the magnetic moment measurements that were also made in this experiment.

The two targets used were made of beryllium to maximize the fraction of high momentum baryons produced. Both were approximately 0.37 interaction lengths long. The upstream target, PC3TGT1, was a cylinder 150 mm long and 6.6 mm in diameter. It was mounted on the upstream end of PC3SW so that it moved in the vertical direction along with the magnet. The second target was 150 mm long and rectangular in shape, with a width of 5.2mm and a height of 5.3mm. It was mounted on the upstream end of magnet PC3ANA. Both targets were mounted on motorized carriers with position sensors that allowed both targets to be moved horizontally. This allowed either target to be removed from the beam during the performance of background studies.

Segmented Wire Ion Chambers (SWICs) were used to monitor the beam position and thus determine the production angle. Three SWICs, PC3WC2, PC3WC3, and PC3WC4, each with 0.5 mm wire spacing, were used to monitor the position of the beam. The locations of these SWICs are shown in Figure 2.1. PC3WC2 was located between magnets PC3V1 and PC3V2 and was used to measure the production angle. PC3WC3 was located in front of the upstream target and was mounted on magnet PC3SW so that it moved with the magnet as it was raised or lowered. PC3WC4 was mounted in front of the second target.

A secondary emission monitor (SEM) was used to monitor the proton beam. The SEM provided a measure of the intensity of the proton beam in the Proton Center beamline. The SEM reading for each spill was recorded on our data tapes. Together,

Plan View

9 mrad

3.86 cm

3.86 cm

731.5 cm

Elevation View

1.14 cm

1.14 cm

731.5 cm

Brass
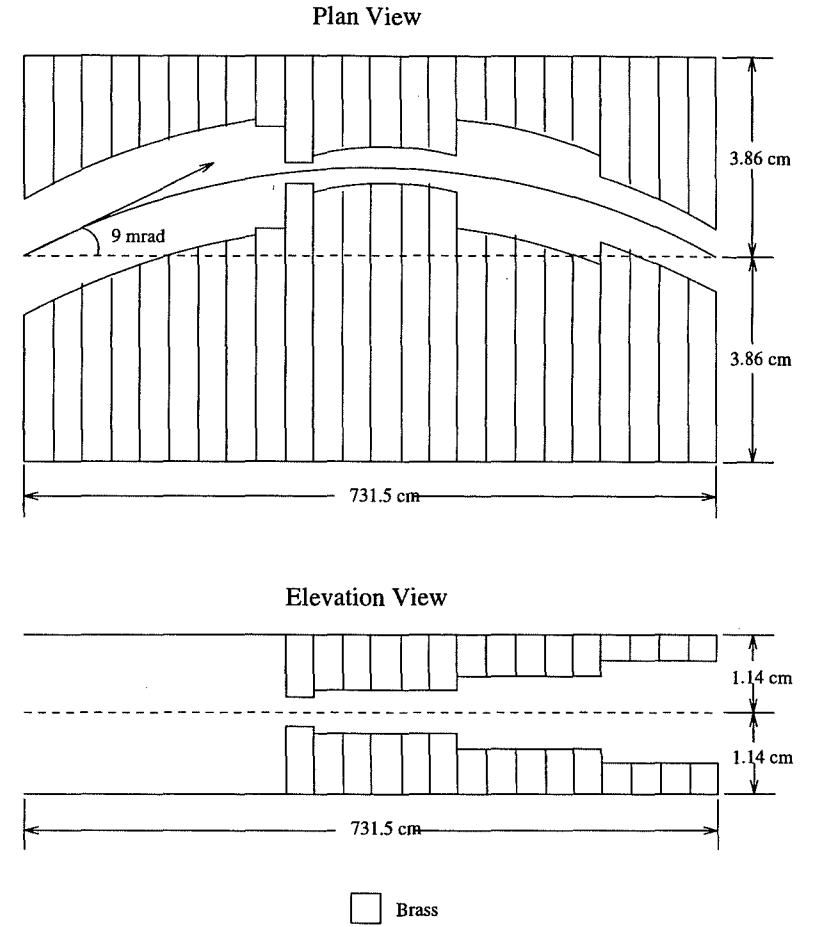
Figure 2.3: The charged collimator in PC3ANA.
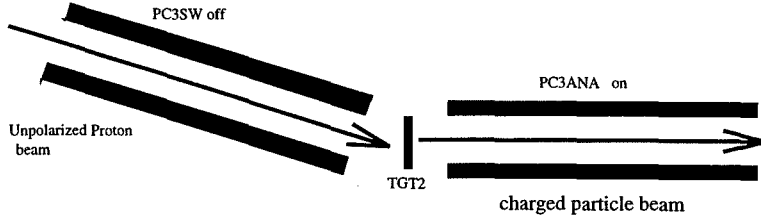
Figure 2.4: The proton production mode.

the SWICs and the SEM provided a means of monitoring the intensity and quality of the proton beam on a spill by spill basis.

2.3 Production Methods

In this experiment there were three different production modes: proton production, unpolarized neutral beam production, and polarized neutral beam production. Figure 2.4 shows how the magnets and targets were arranged for the proton production mode. The upstream target, PC3TGT1 was removed from the beamline, and dipole magnet PC3SW was turned off. In addition, PC3SW was aligned so that the proton beam could pass through the collimator and strike the second target, PC3TGT2, at the desired production angle.

In the unpolarized neutral beam production mode, shown in Figure 2.5, the upstream target, PC3TGT1 was placed in the beam. The protons struck this target at an angle of 0 mr. The particles produced at this target then passed through PC3SW where charged particles were bent out of the beamline. This resulted in a beam of unpolarized neutral particles which then struck the downstream target. As in the proton production modes, PC3SW could be raised or lowered to achieve the desired production angle. Data was taken using this production method at two different settings of the current in charged sweeper magnet, PC3ANA, to take data with a wider range of momentum values.
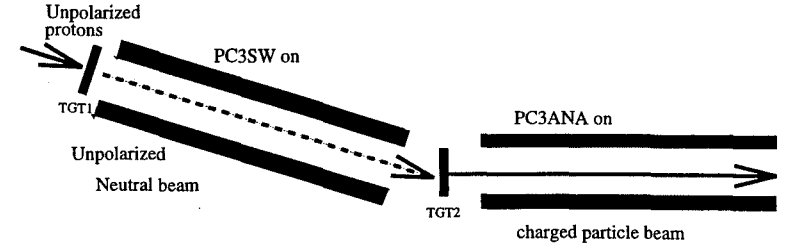
Figure 2.5: The unpolarized neutral beam production mode.
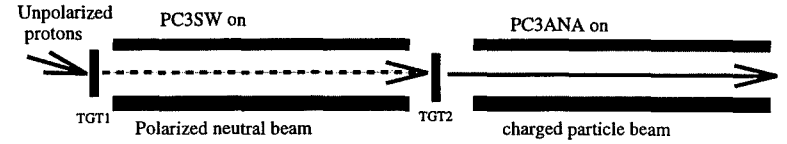
Figure 2.6: The polarized neutral beam production mode.

The polarized neutral beam production mode, shown in Figure 2.6, was similar to the unpolarized neutral beam production mode except that PC3SW always remained horizontal. The protons struck the upstream target at an angle determined by the fields in PC3V1 and PC3V2. The particles produced then entered PC3SW, where the charged particles were bent out of the beamline. The beam that exited PC3SW contained polarized neutral particles which then struck the downstream target at an angle of 0 mrad.

Data was also taken with both production angles at 0 mrad. This was done to produce Ξ^-s and Ω^-s that were known to be unpolarized for use in systematic studies during the polarization analysis. This production mode is similar to that shown in Figure 2.6, except that the protons were incident on PC3TGT1 at 0 mrad.

2.4 Coordinate System

In the spectrometer, positive z-was defined as the direction tangent to the central orbit of the charged collimator at its downstream exit. Positive y was defined to be up, and x was defined such that the coordinate system was right-handed as shown in Figure 2.7. The origin of this coordinate system was based at the exit of the Hyperon magnet collimator. The sign of the production angle was defined by the sign of $\vec{P}_{beam} \times \vec{p}_{\Xi^-}$ in a right handed coordinate system with its origin at the downstream target.

2.5 The Spectrometer

After exiting the Hyperon magnet collimator, the particles entered the spectrometer, which was designed to detect the three-track decays $\Omega^- \to \Lambda + K^-$ and $\Xi^- \to \Lambda + \pi^-$ each with a subsequent $\Lambda \to p + \pi^-$ decay. The spectrometer consisted of four planes of silicon strip detectors (SSDs) in each view (x and y) to track the parent hyperon or its charged daughter, several scintillation counters to provide fast trigger signals, and twelve multiwire proportional chambers (MWPCs) to provide tracking information about the decay products. Figure 2.7 shows the spectrometer, and Table 2.1 lists all the elements of the spectrometer and gives their sizes and positions relative to the exit of the Hyperon magnet. Two dipole analyzing magnets were used to determine the momentum of the daughter protons, pions and kaons. Helium filled bags and tubes were placed between the MWPCs to reduce multiple scattering of the daughter particles. The total amount of material in the beamline was 9.55×10^{-2} interaction lengths.
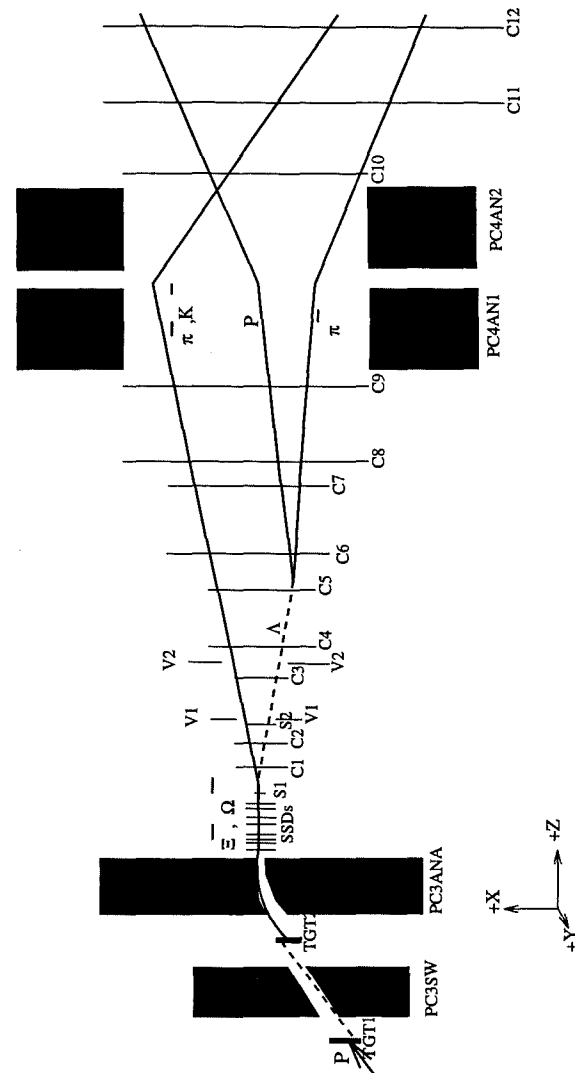
Figure 2.7: Plan view of the E800 spectrometer (not to scale). Also shown is a typical Ξ^- decay.

Detector	Position	Width	Height	Thickness	Pitch	Device Type
SSD1(x)	74.43	2.8	2.8	0.03	.01	SSD
SSD1(y)	79.22	2.8	2.8	0.03	.01	SSD
SSD2(x)	100.97	2.8	2.8	0.03	.01	SSD
SSD2(y)	109.97	2.8	2.8	0.03	.01	SSD
SSD3(x)	129.46	2.8	2.8	0.03	.01	SSD
SSD3(y)	137.80	2.8	2.8	0.03	.01	SSD
SSD4(x)	158.43	2.8	2.8	0.03	.01	SSD
SSD4(y)	166.29	2.8	2.8	0.03	.01	SSD
S1	360.	6.35	3.81	.1	n/a	scintillator
C1(x,y)	561.	12.8	12.8	n/a	1.0	MWPC
C2(x,y)	776.	12.8	12.8	n/a	1.0	MWPC
V1	800.	32.38	8.89	.32	n/a	scintillator
V1(hole)	800.	11.43	6.35	.32	n/a	n/a
S2	800.	10.79	6.35	.1	n/a	scintillator
C3(x,y)	988.	12.8	12.8	n/a	1.0	MWPC
V2	1020.	41.91	11.43	.32	n/a	scintillator
V2(hole)	1020.	13.97	8.25	.32	n/a	n/a
C4(x,y)	1511.	25.6	25.6	n/a	1.0	MWPC
C5(x,y)	2009.	25.6	25.6	n/a	1.0	MWPC
C6(x,y)	2499.	51.2	25.6	n/a	2.0	MWPC
C7(u,v)	3013.	12.8	12.8	n/a	2.0	MWPC
C8(u,v)	3089.	51.2	51.2	n/a	2.0	MWPC
C9(x,y,u)	3697.	51.2	51.2	n/a	2.0	MWPC
C10(x,y)	4261.	63.8	25.6	n/a	2.0	MWPC
C11(x,y)	4840.	128.	38.4	n/a	2.0	MWPC
C12(x,y)	6154.	128.	38.4	n/a	2.0	MWPC

Table 2.1: The size and z positions of the spectrometer elements. All measurements are given in centimeters. Width and height refer to the active area of the detector. (n/a - not applicable)

2.5.1 The Silicon Strip Detectors

The SSDs were the most upstream element of the spectrometer. They were used to accurately track the parent Ξ^-s and Ω^-s before they decayed and also aided in differentiating between the negatively charged daughter from the parent decay and the negatively charged daughter from the Λ^0 decay. There were eight planes of SSDs (manufactured by Hammamatsu) with 0.3 mm thickness and 280 strips of 100 μm pitch. Laben Model MSP1 pre-amplifiers were used to amplify the charge (on the order of 1 fC) collected on a strip when a charged particle passed through it. These pre-amps gave a 1.0 - 2.0 mV output that was amplified and discriminated by Nanometrics Model N-277CD 16 channel amplifier cards. The outputs of the discriminators went into Nanometrics Model N-278 data latches which were read out using the Nanometric Model N-281 CAMAC read-out system. The sensitivity of the MSP1 preamps made them very susceptible to noise, so substantial effort was made to shield data cables and insure that the system was properly grounded. In addition, considerable effort was expended to insure that all components of the Nanometric read-out system functioned properly.

Table 2.2 gives the efficiency of each of the SSD planes for one run. These efficiencies were measured using single track events. To calculate the efficiency of a plane, a track was fit without using that plane, and then the hits in that plane were examined to determine if any of them were within a distance equal to 1.5 times the pitch of the detector from the fit track. The efficiency was defined to be the percentage of the total events with a hit within 1.5 times the pitch of the fit track. In practice, the separation of hits was always quantized by the pitch of the detector plane.

SSD	Efficiency (%)
SSD1(x)	83.
SSD1(y)	63.
SSD2(x)	82.
SSD2(y)	84.
SSD3(x)	81.
SSD3(y)	85.
SSD4(x)	84.
SSD4(y)	82.

Table 2.2: SSD Efficiencies.

2.5.2 The Scintillation Counters

The set of four scintillation counters, S1, V1, S2, and V2 were used to define the beam. The dimensions of these counters are given in Table 2.1. Counters S1 and S2 were used to identify charged particles that were within the beam defined by the hyperon magnet collimator. The veto counters, V1 and V2, had holes in them. The presence of a particle outside the hole region indicated a charged particle that was not from the negative beam region. Counters S1 and S2 had one photomultiplier tube, but because of their center holes, counters V1 and V2 had two photomultiplier tubes, one on either side of the hole. The signals from these two phototubes were logically ORed together to produce one signal for each counter.

The signals from the scintillation counters were discriminated by standard NIM discriminators whose outputs were used in the trigger and were also input to scalers that were read-out at the end of each spill.

2.5.3 The Multiwire Proportional Chambers

Twelve MWPCs were used in the spectrometer. With the exception of C7 and C8, all MWPCs had sense planes in the $\hat{x}$ and $\hat{y}$ directions. The sense planes in C7 and C8 were rotated 45 degrees with respect to the sense planes of the other chambers. These rotated planes are referred to as $\hat{u}$ and $\hat{v}$ planes and were used in the track finding to

match the x and y tracks for each particle. Also, in addition to its x and y planes, C9 had a u sense plane with a 45 degree rotation.

Each MWPC except C9 consisted of three high voltage planes which sandwiched the two sense planes. C9 had four high voltage planes and three sense planes. The sense wires in C1, C2, C3, C4, and C5 had a wire spacing of 1 mm and the other chambers had 2 mm pitch sense planes. Gold plated tungsten wire was used in the sense planes. The high voltage planes in C1, C2, C3, and C5 were made with 0.25 mil thick aluminized mylar foils, and the high voltage planes in the other chambers consisted of 2 or 3 mil copper-beryllium wire at 1mm spacing. C4 and C5 experienced many stability problems during the run, and during the last part of the run, the y sense plane of C5 was disconnected due to excessive sparking.

The gas used in all of the chambers was a mixture of 95% argon, 5% methylal, and 0.12% freon where the percentages are given by gas volume. The correct fraction of methylal was maintained by bubbling the argon - freon mixture through liquid methylal at 2 degrees Celsius. The chamber efficiencies are given in Table 2.3, and were measured using the same method used to measure the SSD efficiencies.

The read-out system for C1, C2, and C3 used LeCroy amplifier-discriminator cards that fed into Nanometric Model N-278 latches. The latches were read-out using the same system used for the SSD hit data. The read-out system for the remaining MW-PCs utilized custom-built electronics. This system consisted of four channel amplifier-discriminator-latch cards from which data was gathered using a "sparse read-out" system[38]. The amplifier cards used in the MWPCs upstream of the analyzing magnets were more sensitive since these chambers were operated at a lower high voltage, which was desirable because of the high particle fluxes in this portion of the spectrometer. In addition, the amplifier cards used in C4 and C5 had their discriminator thresholds lowered so that these chambers could be operated at even lower high voltages. This was done in an effort to improve the efficiency of these detectors, however, their operation

Chamber	Efficiency (%)
C1(x)	94.
C1(y)	93.
C2(x)	92.
C2(y)	94.
C3(x)	95.
C3(y)	95.
C4(x)	69.
C4(y)	67.
C5(x)	93.
C5(y)	94.
C6(x)	98.
C6(y)	99.
C7(u)	94.
C7(v)	98.
C8(u)	96.
C8(v)	98.
C9(x)	96.
C9(y)	97.
C10(x)	98.
C10(y)	100.
C11(x)	95.
C11(y)	97.
C12(x)	96.
C12(y)	97.

Table 2.3: MWPC Efficiencies.

was never totally satisfactory.

2.5.4 The Analyzing Magnets

The magnets between C9 and C10 were used to momentum analyze the charged particles. These magnets were two BM109 dipoles. Both magnets had a x aperture of 61.0 cm. The upstream magnet had a y aperture of 25.4 cm and the downstream magnet had a y aperture of 30.5 cm. Each magnet was 182. cm long and they were separated by a distance of 56. cm. Both magnets had mirror planes to reduce the fringe fields.

The magnetic field of these magnets was determined using two different methods.

First, the "Ziptrack" apparatus was used to make three dimensional field maps of the two magnets. This apparatus was built at Fermilab and uses Hall probes to measure the three magnetic field components at various points inside and outside of the magnet. This apparatus was used to map the field inside the magnet and the fringe field just outside of the magnets. These field maps were used to search for non-homogeneity in the magnets. The fields in both magnets were found to be constant to within a few percent. The second method used the reconstructed masses of the Ξ^-s and Λs to determine the p_T kick of the magnets. This value was found to be -1.445 GeV/c at the standard operating current.

2.6 Trigger

The trigger used to detect three-track events consisted of two parts. The first part used scintillation counters S1, S2, V1, and V2. This trigger required hits in S1 and S2 in conjunction with no hits in V1 and V2 (i.e. $S1 \cdot S2 \cdot \overline{V1} \cdot \overline{V2}$). This insured that a charged particle had entered the spectrometer from the hyperon beam and was not part of a shower from an upstream interaction. This part of the trigger, referred to as the pi trigger, was a very effective way of selecting single track particles which were useful in aligning the spectrometer, monitoring detector efficiency and other systematic studies. For these reasons, pi triggers were written to most of the data tapes at rates that were prescaled to be between 1/32 and 1/1024 of the three-track trigger rate.

The characteristic "V" topology of the Λ that was a daughter of both the Ξ^- and Ω^- decays was used to make a trigger for three-track events. This was done by triggering on charged particles passing through the side of C11 hit by negative pions from the decays and the side of C12 hit by protons from the decays. The complete three track trigger was:

$$S1 \cdot S2 \cdot \overline{V1} \cdot \overline{V2} \cdot (C11)_\pi \cdot (C12)_{proton} \tag{2.1}$$

This was the simplest possible trigger that would still allow us to take data with a reasonable live time (greater that 60%), given the limitations of the readout electronics. The live time is simply the percentage of triggers that were actually readout. A simpler trigger also reduced the possibility of systematic errors due to the trigger. Studies of possible biases due to the trigger are discussed in Chapter 5.

2.7 Data Acquisition System and Experimental Operation

The main consideration during the design of the data acquisition system was maximizing the amount of data that could be collected during one spill. Since the most time consuming process was writing the data to tape, a system in which the data was stored in fast semiconductor memory during the spill and then written to tape during the time between spills was adopted. Figure 2.8 shows a schematic of the data acquisition system.

All of the detectors were read out using a CAMAC system interfaced to a VAXstation Model 3200. When a trigger occurred, a signal was sent to the electronics to prepare for read-out. The trigger also went to a Fermilab designed CAMAC Smart Crate Controller (SCC)[39]. This SCC was designed to execute pre-loaded lists of CAMAC instructions at a rate of 1 MHz. When the SCC received a trigger signal, it executed a list of instructions that read out the data from the SSDs, MWPCs, and various other latches and scalers. This data was written into a fast first-in, first-out (FIFO) memory unit. At the end of each spill, scalers that recorded trigger element hits, the SEM, and other counters were read out. Then, the data in the FIFO was transferred to the VAXstation and written to 8mm video tape. Each data tape held an average of ten data runs, with each run containing about 500,000 events, and each event containing approximately 200 bytes of data. Table 2.4 gives a summary of the
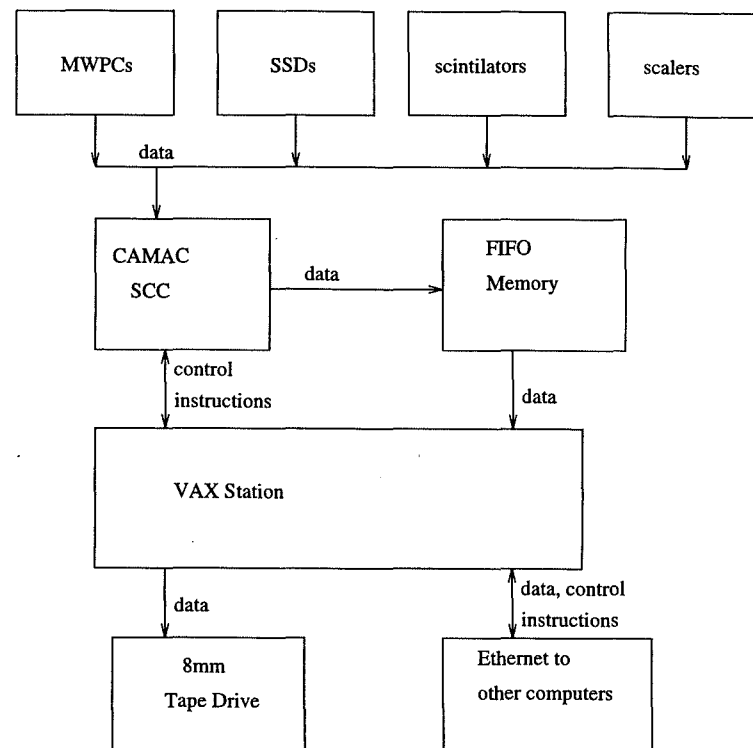
Figure 2.8: The data acquisition system.

Production Mode	Angle	Runs	Three-track Triggers
Unpolarized Neutral Beam	+	711	346,982,603
Hyperon Magnet = −2900	−	757	374,297,889
Unpolarized Neutral Beam	+	308	150,467,562
Hyperon Magnet = −750	−	289	142,700,032
Polarized Neutral Beam	+	182	87,777,817
	−	171	84,086,479
Zero Mrad	+	170	82,531,343
	−	172	84,187,513
Totals		2760	1,353,031,238

Table 2.4: Summary of data collected.

number of data runs and triggers written to tape for each of the various production modes and angles reported on in this thesis. The run size was selected to produce data files that were of a manageable size, and to take approximately 30 minutes, which was thought to be a reasonable interval between checks of the beam positions and other experimental conditions. Under normal operating conditions, each unpolarized neutral beam production run took approximately 20 minutes. Polarized neutral beam runs took approximately 40 minutes due to lower particle production rates. The main factors limiting the data taking rate were radiation loss restrictions in the targeting area and deadtime limitations of the spectrometer. The live time of the experiment was always greater than 60%.

Some fraction of the data that was written to tape was also distributed via ethernet to other computers. These computers performed a quick analysis of the events to monitor the performance of the spectrometer and data acquisition system. The amount of data available for this monitoring was limited by several factors, including network loading, but was usually at least 50%.

During the data runs, the production angle was monitored by observing the beam positions on the SWICs. Also, the number of one track and three track triggers per delivered proton were monitored as an additional check of the spectrometer and beam

position. Magnet currents were monitored and controlled using the Fermilab Epicure beamline control system. The magnet currents and SWIC positions were recorded in the experimental logbooks several times during each data tape.
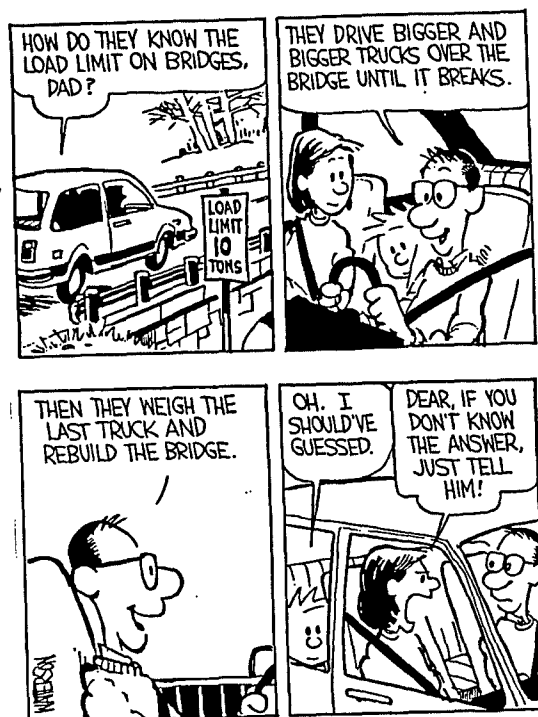
Chapter 3

Event Reconstruction and

Selection

3.1 Introduction

The three charged track topology of the decays $\Xi^- \to \Lambda + \pi^-$ or $\Omega^- \to \Lambda + K^-$, followed by $\Lambda \to p + \pi^-$ allowed the events to be completely reconstructed using only the tracking information from the hits in the MWPCs. The SSD information added additional constraints on the parent track when available. The three tracks in the x view were bent by the momentum analyzing magnet, with the proton, which is the highest momentum track, being bent in the opposite direction from the two negatively charged tracks. Once the three daughter tracks had been reconstructed, they were fit to a Ξ^- or Ω^- hypothesis using geometric and kinematic constraints.

3.2 The First Pass Analysis

An initial pass was made through the raw data tapes to eliminate events which did not have enough information to be successfully reconstructed as three-track events.

Description of Selection Criteria	Percentage of Raw Three-track Triggers Eliminated
Less than 2 hits in 3 planes of C6 and C8	62.5
Less than 3 hits in C7 and C8 and less than 2 hits in C9u	0.0
Less than 2 hits in 2 x-planes of C10, C11, or C12	2.8
Less than 2 hits in 3 y-planes of C6, C7, C8, C9, C10, C11, or C12	5.5

Table 3.1: Selection criteria for first pass reconstruction. These percentages are for a typical unpolarized neutral beam production data run.

Production Mode	Angle	Runs	Three-track Triggers	Three-track Candidates
Unpolarized Neutral Beam Hyperon Magnet = −2900	+	711	346,982,603	102,177,861
	−	757	374,297,889	110,232,099
Unpolarized Neutral Beam Hyperon Magnet = −750	+	308	150,467,562	46,929,723
	−	289	142,700,032	45,346,166
Polarized Neutral Beam	+	182	87,777,817	34,212,605
	−	171	84086,479	30,240,120
Zero Mrad	+	170	82,531,343	38,000,350
	−	172	84,187,513	39,097,574
Totals		2760	1,353,031,238	446,236,498

Table 3.2: Summary of data remaining after first pass.

Table 3.1 shows the criteria used and the percentage of events eliminated by each selection criteria.

The raw data from events that passed these selection criteria were written to first level summary tapes. Table 3.2 shows the number of three-track events remaining for each data taking mode after this step. This pass removed 67% of the raw triggers from the three-track data sample. In addition, events that passed the criteria of a good single track event were written to a separate set of tapes for use in calibrating and aligning the experiment.

3.3 The Reconstruction Program

The reconstruction program was a multi-step process starting from the first level summary data described above. Figure 3.1 shows a schematic diagram of the overall reconstruction process. In this experiment it was very important that the reconstruction program mis-reconstruct as few events as possible since any incorrectly reconstructed event could have a noticeable effect on the measured asymmetries. In addition it was important that the efficiency of the reconstruction process not vary appreciably over the range of selected events. To do this, three different reconstruction methods were used. The different methods each had their strengths and weaknesses, but by combining the three methods, their weaknesses could be minimized.

The first stage of the reconstruction process involved additional hit counting criteria to remove events that Monte Carlo studies showed were difficult to reconstruct correctly. These selection criteria and the corresponding percentage of events each eliminated are given in Table 3.3.

Description of Selection Criteria	Percentage of First Level Summary Events Eliminated
Two or more hits in the y views of C6, C9, and C10	4.2
Two or more hits in the x views of C6, C9, C10, and C11	23.1
Fewer than 3 planes of C6 - C12 have more than four hits	28.1

Table 3.3: Hit counting data selection criteria. These percentages are for a typical unpolarized neutral beam production data run.

3.3.1 Initial Reconstruction Program

Any event that survived these hit counting criteria was passed to the basic three-track reconstruction program. This program began by looking at the hits in five of the 2mm chambers (C6,C9,C10,C11,C12). The y tracks were found first since they were straight while the x tracks were bent by the analysis magnets. If three y tracks were found, the
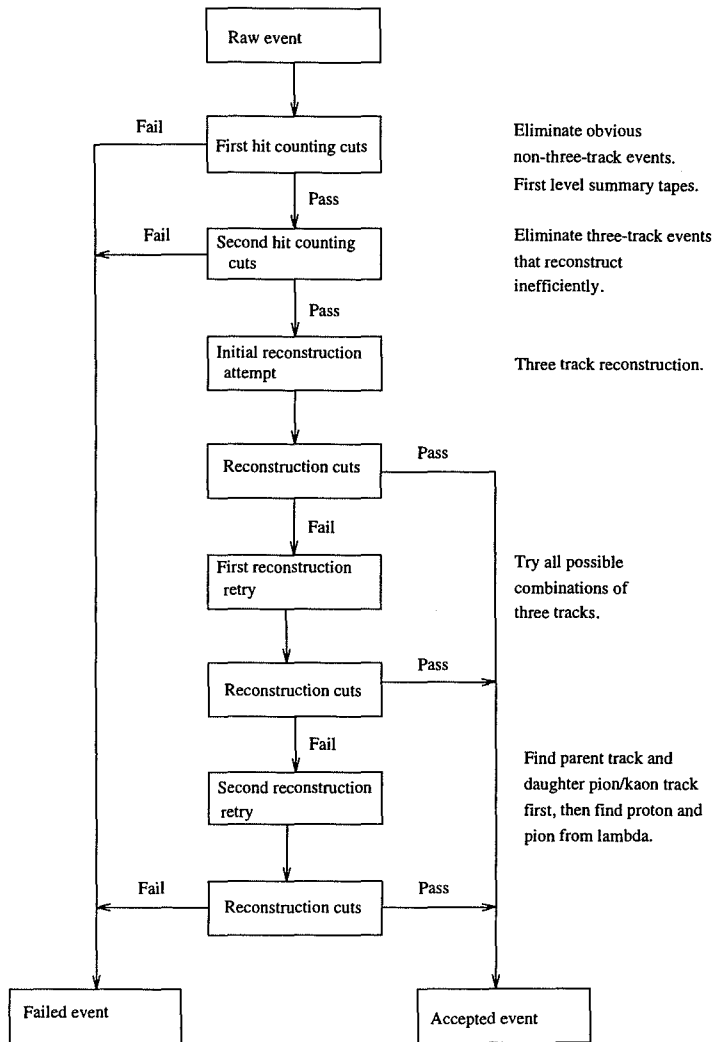
Figure 3.1: The reconstruction process.

program next looked for three tracks in the x view of the 2mm chambers upstream of the analysis magnets. Then, the x and y tracks were matched using the information from the u and v planes of C7, C8, and C9. Finally, three x tracks were found in the chambers downstream of the analysis magnets and matched with the upstream tracks at the magnet bendplane.

Next, an attempt was made to find the parent track in the SSDs, and then hits from the 1mm chambers (C1, C2, C3, C4, and C5) were added to the parent and daughter tracks. Accepted events were not required to have a parent track, however, the parent track did help reduce the uncertainty in the parent vertex measurement. Then, the daughter tracks for any successful solutions were fit to a three-track topology in both views simultaneously. The fitting routine calculated the location of the Ξ^- or Ω^- and Λ vertices, the momentum vectors of all the particles involved in the decay, the position of the parent particle at the target, X_T and Y_T, and the mass of the parent particle using both a Ξ^- and Ω^- hypothesis. In addition, the fitting routine calculated a geometric chi-squared per degree of freedom, χ^2_G/DF, which was used to judge how well the event was fit.

The final part of this procedure varied the proton and π momentum vectors within their uncertainties to force the Λ to have the correct mass. This procedure calculated a parameter, χ^2_Λ, which was a measure of the difference between the Λ solution for the three-track, two-vertex fit and the solution with the correct mass, and was used as another data selection criteria.

All events that were successfully reconstructed by this procedure were required to pass a set of data selection criteria that were intended to remove background and badly reconstructed events. These data selection criteria are listed in Table 3.4.

Any events that passed these selection criteria were accepted as correctly reconstructed events. Of the final unpolarized neutral beam production events used in the

Description of Data Selection Criteria	Real Events Removed	Monte Carlo Removed
mass within 15 MeV of m_{Ξ^-} or m_{Ω^-}	40.8%	33.5%
$\chi^2{}_G/DF < 4$	2.9%	4.0%
$\chi^2{}_\Lambda < 15$	5.0%	5.3%
$|X_T| < 0.9 cm$ $|Y_T| < 0.8 cm$	2.0%	1.8%
no hits used on more than one track at least 2 hits used in C6, C9, C10, and C11 x at least 2 hits used in C6, C9, and C10 y	45.7%	46.3%

Table 3.4: Reconstructed data selection criteria.

polarization analysis, 67.3% were accepted by this reconstruction pass. When Monte Carlo data was analyzed, this reconstruction pass contributed 70.5% of the accepted events.

3.3.2 First Reconstruction Retry

All events which passed the initial hit counting criteria, but could not be successfully reconstructed by the initial reconstruction program were reprocessed using a different track finding method.

This track finding method first found all possible tracks in the y views of C6, C8, and C10. Any track would not lead to a valid solution were not considered. For example, tracks that pointed outside the analysis magnet apertures were eliminated. From the tracks that remained, sets of three tracks were selected as possible tracks from the Ξ^- or Ω^- decay. The two tracks assigned as the Λ daughter particles were required to have a vertex upstream of C6. Next, all possible upstream and downstream x tracks were constructed. Any upstream and downstream x tracks which intersected the bendplane of the analysis magnets within 0.5 cm of each other were joined, and then the x and y tracks were matched using hits from the u and v planes of C7, C8, and C9.

All possible combinations of three matched x and y tracks were made and each

of these sets of solutions was then passed through a series of fitting routines that eliminated solutions with incorrect hit assignments. The first fitting routine required that the two tracks that were thought to correspond to the Λ daughter particles have a good geometric fit to the Λ topology. This fitting routine was able to reject incorrect solutions quickly because the algebra required to fit the Λ topology was exactly soluble.

Solutions that survived these fitting routines were then passed to the geometric three-track fitter described in section 3.3.1. Solutions with values of $\chi^2{}_G/DF < 10$ were then passed to the kinematic Λ fitter used in the initial reconstruction pass (section 3.3.1), and solutions with $\chi^2{}_\Lambda > 100$ were eliminated.

Next, an attempt was made to add additional hits from the 1mm chambers, and then the geometric three-track fit was redone. The solution was then required to pass the data selection criteria in Table 3.4. If more than one possible solution remained, the solution with the smallest $\chi^2{}_G/DF$ was found and any solution with $\chi^2{}_G/DF$ more than 0.2 above this minimum was rejected. From the remaining solutions, the one with the lowest $\chi^2{}_\Lambda$ was selected. The portion of the final unpolarized neutral beam data sample reconstructed by this retry method was 19.5%. When analyzing Monte Carlo data, 15.3% of the accepted sample came from this retry process.

3.3.3 Second Retry Method

At this point in the reconstruction process, any event that had not been successfully reconstructed by either the initial reconstruction program or the first retry was sent to a second and final retry program. This program used a different approach to the problem of correctly assigning the hits to the various tracks. Instead of trying to find the tracks corresponding to the daughter particles first, this approach first looked for the parent track in the SSDs and the most upstream 1mm chambers. It then used the knowledge that one of the daughter tracks would originate at the Ξ^- or Ω^- vertex and

Production Mode	Angle	Three-track Candidates	Ξ^- Candidates	Ω^- Candidates
Unpolarized Neutral Beam	+	102,177,861	14,474,537	1,822,051
Hyperon Magnet $= -2900$	−	110,232,099	14,886,637	1,873,727
Unpolarized Neutral Beam	+	46,929,723	5,510,850	765,328
Hyperon Magnet $= -750$	−	45,346,166	5,238,496	726,001
Polarized Neutral Beam	+	34,212,605	1,201,471	155,917
	−	30,340,120	1,275,716	161,010
Zero Mrad	+	38,000,350	1,818,638	223,249
	−	39,097,574	1,875,620	230,205
Totals		446,236,498	46,281,965	5,957,488

Table 3.5: Summary of data remaining after the reconstruction pass.

therefore should intersect the parent track. Typically, one or two possible solutions for the daughter K^- (π^-) from the Ω^- (Ξ^-) were found, and for each solution, the remaining hits were used in an attempt to fit a Λ.

When a good Λ solution was found, the event was passed through the geometric and kinematic fitters described in section 3.3.1. Next, the data selection criteria from Table 3.4 were imposed. If more than one good solution for an event was found, the best solution was selected using the same method utilized in section 3.3.2. This retry contributed 13.2% of the events in the reconstructed unpolarized neutral beam data sample. When Monte Carlo data was analyzed, this retry contributed 14.2% of the accepted sample.

Table 3.5 shows the total number of reconstructed events that were accepted under both the Ξ^- and Ω^- mass hypothesis.

3.4 The Monte Carlo Program

A Monte Carlo program was developed to simulate real data events as closely as possible. This program was used for many different tasks, including designing the experiment, testing the reconstruction program, studying data selection criteria, and studying

experimental backgrounds. It was not directly used in the analysis of the data.

In the Monte Carlo program, the parent particle was generated in the downstream target using a Gaussian distribution in x and y. The parent particle momentum was produced with a spectrum that matched the momentum spectrum of the real data sample.

The parent particles were then traced through the charged collimator and any that exited the collimator were allowed to randomly decay with their known lifetimes[40]. All subsequent unstable daughter particles were also allowed to decay randomly according to their known lifetimes. The daughter particles were then tracked through the spectrometer and bent in the momentum analyzing magnets.

The x and y position of each charged particle was calculated at each MWPC and SSD signal plane. Using this information and the chamber centers found from alignment studies, wire hits were generated for each charged track. The events were then required to pass the experimental trigger conditions. The hit wire information for events that passed the trigger conditions was written to files in the same format as the first level summary tapes. In addition, other information about the events, including generated kinematic parameters and information about the hit assignments were written to other files for use in checking the efficiency of the reconstruction and analysis programs.

In addition to generating "perfect" Monte Carlo events, it was possible to generate more realistic Monte Carlo events to make more detailed studies of the experimental acceptances. To do this, several other features were added to the program. Coulomb multiple scattering of the particles on the material in the spectrometer was one of the added features. The position and corresponding radiation lengths of the material in the spectrometer was compiled, and a random number generator was used to determine if a particle was scattered by some part of the apparatus. When scattering occurred,

the direction of the particle was adjusted and tracking of the particle through the spectrometer continued. Studies of real data also revealed that a particle passing through a plane of a detector could cause two adjacent wires to register hits if the track passed through the central region between the two wires. The frequency of such occurrences was studied with real data and simulated in the Monte Carlo. The MWPC and SSD efficiencies discussed in Chapter 2 were also incorporated into the Monte Carlo program. Also, the existence of fringe fields in the Hyperon magnet and the analysis magnets, and their effect on the direction of charged particle tracks were studied and simulated.

It should be noted that the purpose of the Monte Carlo program was not to model the data in every possible detail. Rather it was intended to be a useful tool in understanding the experiment and the various reconstruction programs.

3.5   Monte Carlo Program Performance

To ensure that the Monte-Carlo-generated events accurately mocked the real data, comparisons were made between reconstructed Monte Carlo events and reconstructed real data events. Figures 3.2 - 3.5 show comparisons of m_{Ξ^-}, X_T, Y_T, the Ξ^- and Λ vertices, the Ξ^- and Λ momentum spectra, χ^2_G/DF, and χ^2_Λ. These plots demonstrate that the Monte-Carlo-generated events adequately matched the real data events.

3.6   Performance of the Reconstruction Process

One reason that two retry processes were developed to improve the reconstruction can be see in Figure 3.6. This shows the difference between the Monte-Carlo-generated value and the reconstructed value of the center of mass decay angles on an event by event basis. In making this plot, only the first reconstruction process was used. These plots show that while this process generally does a good job of reproducing the generated
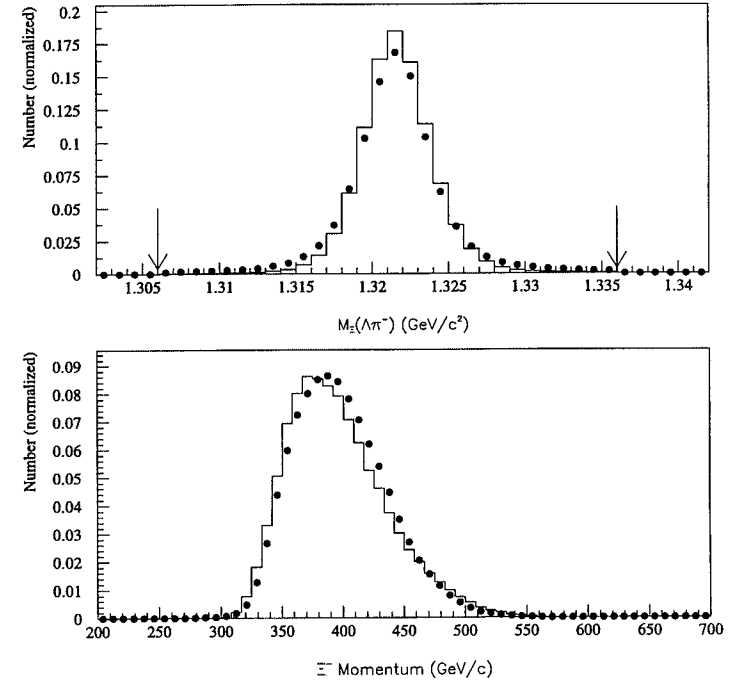
Figure 3.2: Comparison of Ξ^- mass and momentum for Monte Carlo (solid line) and real data (circles). The arrows indicate the data selection criteria.
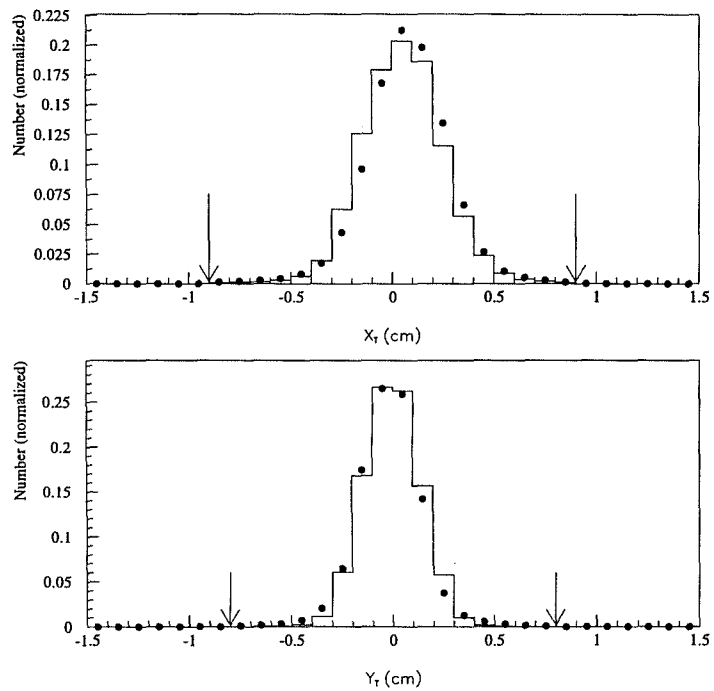
Figure 3.3: Comparison of x and y distributions at the downstream target for Ξ^- events for Monte Carlo (solid line)and real data (circles). The arrows indicate the data selection criteria.
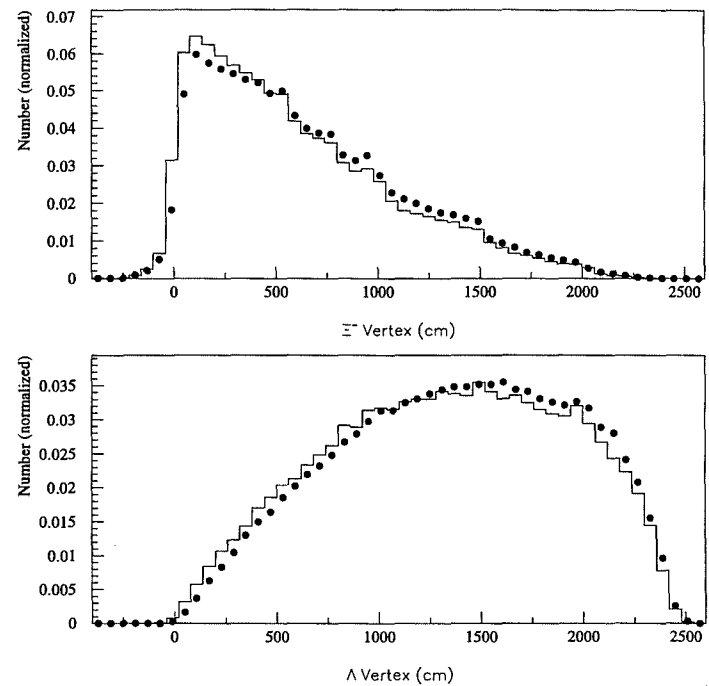
Figure 3.4: Comparison of Ξ^- and daughter Λ vertex distributions for Monte Carlo (solid line) and real data (circles).
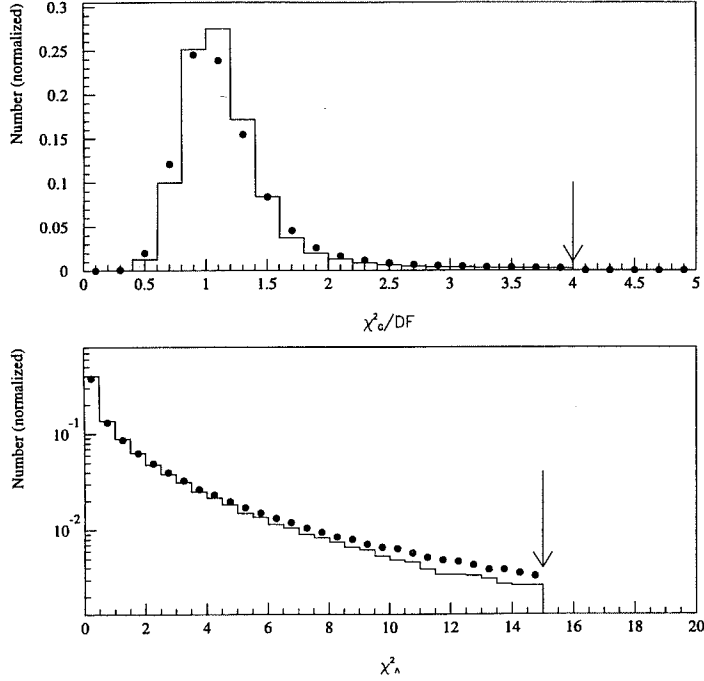
Figure 3.5: Comparison of χ^2_G/DF and χ^2_Λ distributions for Monte Carlo (solid line) and real data (circles) Ξ^- events.

cosine value, approximately 10% of the events are badly reconstructed. The main reason for this mismatch in the cosine distributions is problems with hit selection in the first reconstruction process. A comparison to the original Monte Carlo event information shows that only about 89% of the accepted events had the correct track assignment. In the polarization analysis, these mis-reconstructed events could have a substantial effect on the measured polarization.

It was found that the data selection criteria involving $\chi^2{}_G/DF$, $\chi^2{}_\Lambda$, X_T, Y_T, and the parent mass, listed in Table 3.4, increased the percentage of events with correct hit assignment to about 98%. These new selection criteria reduced the number of accepted Monte Carlo events from 60% to 37%.

The idea behind the two additional retry passes was to increase the percentage of events accepted by the reconstruction, especially events with small opening angles, without increasing the number of events with misassigned hits. The results of this effort are shown in Figure 3.7. This plot shows that now almost 100% of the events have their cosine values properly reconstructed. In addition, 51% of the Monte Carlo events that satisfied the criteria in Table 3.1 were accepted, and the percentage of events that had hit assignment problems was not increased.

To further study the effectiveness of the overall reconstruction process, extensive studies were made to ensure that the reconstruction adequately reproduced the Monte-Carlo-generated properties of the events. Comparisons were made between the Monte Carlo generated and reconstructed values of the Ξ^- and Λ vertex positions along the z-axis, and the Ξ^- and Λ momenta. Similar comparisons were made using Monte Carlo generated Ω^- events. It was found that the reconstruction process was able to adequately reproduce the Monte Carlo generated quantities.
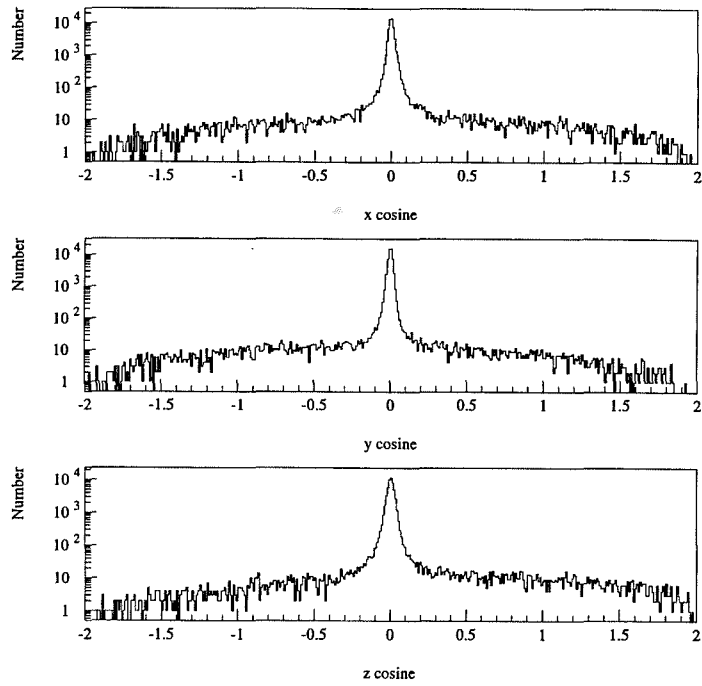
Figure 3.6: Difference between generated and reconstructed cosine values using only the first reconstruction process.
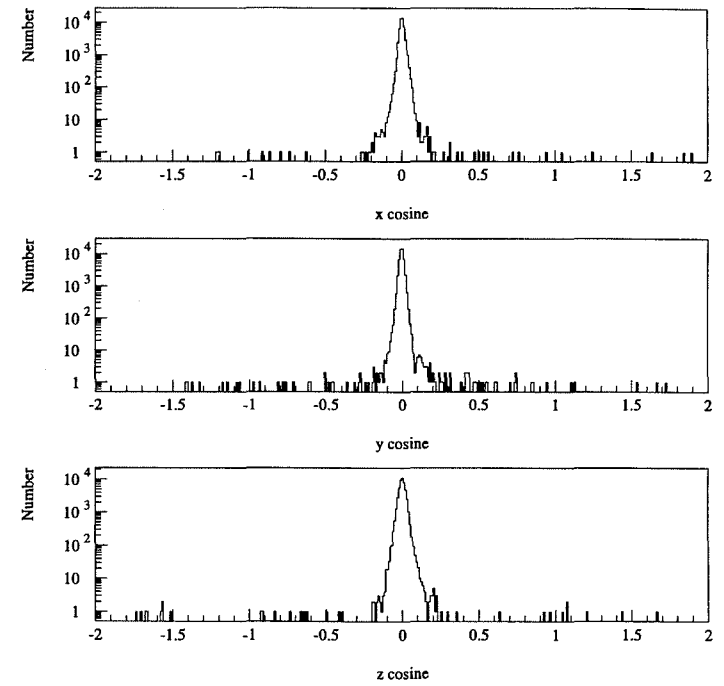
Figure 3.7: Difference between generated and reconstructed cosine values using all parts of the reconstruction process.
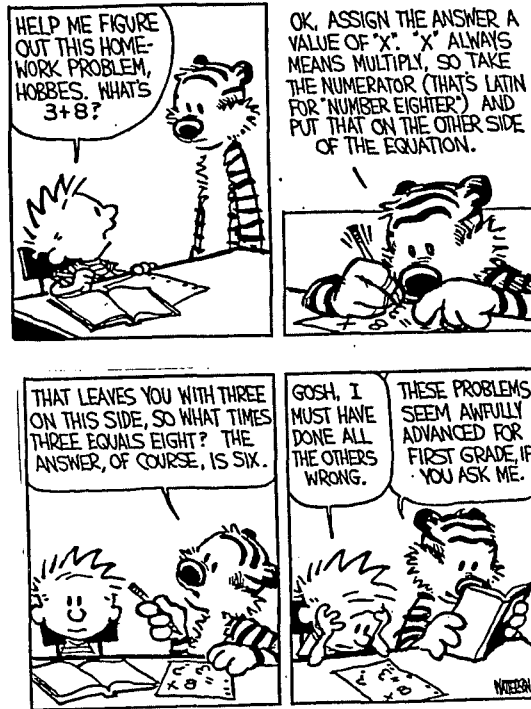
Chapter 4

Polarization Analysis

4.1 Ξ^- Polarization

The decays $\Xi^- \to \Lambda + \pi^-$ and $\Lambda \to p + \pi^-$ both involve the decay of a spin $\frac{1}{2}$ particle into a spin $\frac{1}{2}$ particle and a spin 0 particle. As a result, the distributions of the daughter baryon in the rest frame of the parent, $\frac{dn}{d\Omega}$, obeys the following equation:

$$\frac{dn}{d\Omega} = \frac{1}{4\pi}(1 + \alpha \vec{P} \cdot \hat{p}) \tag{4.1}$$

Here, $\vec{P}$ is the parent polarization, $\hat{p}$ is the direction of the daughter spin $\frac{1}{2}$ particle in the rest frame of the parent, and α is the parity violating helicity of the daughter spin $\frac{1}{2}$ particle[41]. This equation shows that unpolarized particles decay isotropically. Expressing Equation 4.1 in spherical coordinates and integrating over the azimuthal angle, ϕ, yields

$$\frac{dn}{d(cos\theta_i)} = \frac{1}{2}(1 + \alpha P_i cos\theta_i) \tag{4.2}$$

where P_i is the component of the polarization along axis $\hat{i}$, and θ_i is the angle between the daughter particle direction and axis $\hat{i}$. The integration over ϕ that led to Equation 4.2 is only experimentally useful if there is little or no dependence of the daughter distribution on ϕ due to apparatus acceptance.

Since the acceptance of the Λ decay products was well understood, the measurement of the Ξ^- polarization was done by directly measuring the Λ polarization. $\vec{P}_\Lambda$ and $\vec{P}_\Xi$ are related by the equation[42]:

$$\vec{P}_\Lambda = \frac{(\alpha_\Xi + \hat{\Lambda} \cdot \vec{P}_\Xi)\hat{\Lambda} + \beta_\Xi(\vec{P}_\Xi \times \hat{\Lambda}) + \gamma_\Xi(\hat{\Lambda} \times \vec{P}_\Xi) \times \hat{\Lambda}}{1 + \alpha_\Xi \hat{\Lambda} \cdot \vec{P}_\Xi} \quad (4.3)$$

Here, $\hat{\Lambda}$ is the direction of the Λ in the Ξ^- rest frame and $\vec{P}_\Xi$ is the Ξ^- polarization. α_Ξ, β_Ξ, and γ_Ξ are the weak decay parameters for $\Xi^- \rightarrow \Lambda + \pi^-$ and obey the relation

$$\alpha_\Xi{}^2 + \beta_\Xi{}^2 + \gamma_\Xi{}^2 = 1 \quad (4.4)$$

It should be noted that a vector polarization is really only well defined in the rest frame of the polarized particle. Therefore, the quantities on the right hand side of Equation 4.3 are measured in the Ξ^- rest frame, and $\vec{P}_\Lambda$ is defined in the Λ rest frame. This equation can be simplified by assuming time reversal invariance which implies $\beta_\Xi = 0$[43]. After making this substitution and rearranging terms, Equation 4.3 becomes:

$$\vec{P}_\Lambda = \frac{\alpha_\Xi \hat{\Lambda} + ((1 - \gamma_\Xi)\hat{\Lambda} \cdot \vec{P}_\Xi)\hat{\Lambda} + \gamma_\Xi \vec{P}_\Xi}{1 + \alpha_\Xi \hat{\Lambda} \cdot \vec{P}_\Xi} \quad (4.5)$$

This equation shows that a sample of unpolarized Ξ^-s can yield a sample of polarized Λs if the axes are selected in such a manner that the average value of $\hat{\Lambda}$ is large. If the average value of $\hat{\Lambda}$ is small, this term could be neglected.

Since the polarization was measured with respect to the spectrometer axes, and since $\hat{\Lambda}$ should be a random direction with respect to the spectrometer axes, terms involving $\hat{\Lambda} \cdot \vec{P}_\Xi$ should be small. Neglecting these terms in Equation 4.5 leads to a much simpler expression:

$$\vec{P}_\Lambda = \alpha_\Xi \hat{\Lambda} + \gamma_\Xi \vec{P}_\Xi \quad (4.6)$$

4.2 Ω^- Polarization

A similar expression can be derived to relate the polarization of the Ω^- to the polarization of its daughter Λ. This derivation is complicated by the fact that the Ω^- is not

a spin $\frac{1}{2}$ particle. The spin of the Ω^- has not actually been measured, but a spin of $\frac{3}{2}$ is predicted by the standard quark model and a spin of $\frac{1}{2}$ has been ruled out by experimental evidence[44, 45]. In this analysis, we assume a value of $\frac{3}{2}$. The relationship between $\vec{P}_\Omega$ and $\vec{P}_\Lambda$ is[25, 46, 47]

$$\vec{P}_\Lambda = \frac{1}{5}(1 + 4\gamma_\Omega)\vec{P}_\Omega \quad (4.7)$$

Since α_Ω is small [40] and time reversal invariance implies $\beta_\Omega = 0$, Equation 4.4 leads to the conclusion that $|\gamma_\Omega| \approx 1$. With this substitution, Equation 4.7 reduces to

$$\vec{P}_\Lambda = \begin{cases} \vec{P}_\Omega & \text{for } \gamma_\Omega = 1 \\ -0.6\vec{P}_\Omega & \text{for } \gamma_\Omega = -1 \end{cases} \quad (4.8)$$

A value of $\gamma_\Omega = +1$ is predicted by theory [48, 49, 50] and favored by the data from this experiment [47].

4.3 Λ Polarization Measurement

The Λ polarization was measured by observing the distribution of the daughter protons from the decay $\Lambda \rightarrow p + \pi^-$. For this decay, Equation 4.2 becomes:

$$\frac{dn_p}{d(cos\theta_i)} = \frac{1}{2}(1 + \alpha_\Lambda P_{\Lambda i} cos\theta_i) \quad (4.9)$$

This can be combined with Equation 4.6 to get

$$\frac{dn_p}{d(cos\theta_i)} = \frac{1}{2}[1 + (\alpha_\Lambda \alpha_\Xi \Lambda_i + \alpha_\Lambda \gamma_\Xi P_{\Xi i})cos\theta_i] \quad (4.10)$$

Here, $P_{\Xi i}$ and Λ_i are the components of $\vec{P}_\Xi$ and $\hat{\Lambda}$ along axis $\hat{i}$.

Combining Equation 4.8 with Equation 4.9, leads to a similar expression for the Ω^- case.

$$\frac{dn_p}{d(cos\theta_i)} = \frac{1}{2}[1 + \alpha_\Lambda P_{\Omega i} cos\theta_i] \quad (4.11)$$

If the experimental apparatus and reconstruction programs both had perfect acceptances, $\vec{P}_\Xi$ and $\vec{P}_\Omega$ could be found by fitting the proton distribution to Equations 4.10 and 4.11 and finding the values of the polarizations that gave the best fit. However, this is not the case and a method of correcting for the finite acceptance of the spectrometer and reconstruction must be used.

A hybrid Monte Carlo technique[51] was used to map out the experimental acceptance in $cos\theta_i$ using fake events. These fake events were kinematically identical to a given real event in every way except that the value of $cos\theta_i$ was randomly chosen between −1 and +1. They were required to pass through the same data selection criteria used on real data events. These criteria included known chamber apertures and topology requirements. The topology criteria are discussed in further detail in Appendix B. In addition to these selection criteria, a map of wires in the MWPCs that were very noisy or never registered hits was compiled and any fake event hit that fell on one of these wires was removed. For every real event, fake events were generated until 10 such events passed the selection criteria. Statistical studies indicated that the requirement of 10 accepted hybrid events would be large enough to allow the sampling uncertainties due to the hybrid Monte Carlo to be neglected in comparison to the statistical uncertainties of the real data.

When $P_{\Lambda i} = 0$, the fake distribution was expected to agree with the real $cos\theta_i$ distribution since both sets of events would have passed through the same data selection criteria. When $P_{\Lambda i} \neq 0$, however, the distributions will not match due to the asymmetric $cos\theta_i$ distribution of the real data events. To correct this, Equation 4.10 was used to generate a weighting factor, W_{jk}, for each fake event.

$$W_{jk} = \frac{1 + (\alpha_\Lambda \alpha_\Xi \hat{\Lambda}_i + \alpha_\Lambda \gamma_\Xi P_{\Xi i}) cos\theta_{ijk}}{1 + (\alpha_\Lambda \alpha_\Xi \hat{\Lambda}_i + \alpha_\Lambda \gamma_\Xi P_{\Xi i}) cos\theta_{ij}} \qquad (4.12)$$

where subscript j refers to the real event, and subscript jk refers to the kth fake event generated for real event j. A similar expression for the P_Ω analysis was derived from

Equation 4.11.

$$W_{jk} = \frac{1 + \alpha_\Lambda P_{\Omega i} cos\theta_{ijk}}{1 + \alpha_\Lambda P_{\Omega i} cos\theta_{ij}} \qquad (4.13)$$

The $cos\theta_i$ distributions were divided into twenty bins, and a bin by bin comparison of the real and fake $cos\theta_i$ distributions was made. A χ^2 was calculated for each bin using the following equation

$$\chi^2 = \frac{(n_r - n_f N_r/N_f)^2}{n_r} \qquad (4.14)$$

where n_r and n_f are the contents of a given $cos\theta_i$ bin for the real and fake distributions respectively. N_r and N_f are the total number of events in the real and fake distributions. For a given bin, n_f is given by

$$n_f = \sum_{jk} W_{jk} \qquad (4.15)$$

The overall χ^2 is calculated by summing the χ^2s from the individual bins. The polarization, $P_{\Xi i}$ is then varied to find the minimum χ^2. Equation 4.12 is expanded as a power series in $\alpha_\Lambda \gamma_\Xi P_{\Xi i}$ and substituted into Equation 4.15 so that

$$n_f = \sum_{jk} W_{jk} = \left[\sum_{jk} A_{jk}\right] + \left[\sum_{jk} B_{jk}\right] (\alpha_\Lambda \gamma_\Xi P_{\Xi i}) - \left[\sum_{jk} C_{jk}\right] (\alpha_\Lambda \gamma_\Xi P_{\Xi i})^2 + \cdots \quad (4.16)$$

where

$$A_{jk} = \frac{1 + \alpha_\Lambda \alpha_\Xi \hat{\Lambda}_i cos\theta_{jk}}{1 + \alpha_\Lambda \alpha_\Xi \hat{\Lambda}_i cos\theta_j} \qquad (4.17)$$

$$B_{jk} = \frac{cos\theta_{jk} - cos\theta_j}{(1 + \alpha_\Lambda \alpha_\Xi \hat{\Lambda}_i cos\theta_j)^2} \qquad (4.18)$$

$$C_{jk} = \frac{cos\theta_j(cos\theta_{jk} - cos\theta_j)}{(1 + \alpha_\Lambda \alpha_\Xi \hat{\Lambda}_i cos\theta_j)^3} \qquad (4.19)$$

The sums in Equation 4.16 are not dependent on $P_{\Xi i}$ so a single pass can be made through the events to evaluate the sums, and then $P_{\Xi i}$ can be varied to minimize the overall χ^2. The uncertainty in the measurement of $P_{\Xi i}$ is evaluated by varying $P_{\Xi i}$ on either side of the best value until the overall χ^2 changes by 1 from the minimum value.

Once a value has been found for $P_{\Xi i}$, a second pass through the hybrid Monte Carlo was then made, using this value of $\vec{P}_\Xi$ to consider the $\hat{\Lambda} \cdot \vec{P}_\Xi$ terms in Equation 4.5 that were neglected in the first pass. New weights, W_{jk}, were calculated and the power series expansion was repeated to find a new value of $P_{\Xi i}$. It was found that no more than one iteration was needed for the value of $\vec{P}_\Xi$ to converge. The measurement of P_Ω was performed using the same technique.

This analysis method was tested using Monte Carlo data that was generated to simulate a polarized data sample. It was found that the analysis process adequately reproduced that input polarization. This will be discussed further in Chapter 5.

4.4 The Bias Cancellation

The method described above only accounts for the geometric acceptance of the spectrometer and for the data selection criteria imposed on the real data sample. It does not account for acceptances due to other reconstruction acceptances or effects due to multiple scattering or any unidentified processes. The value of the asymmetry, $\alpha_\Lambda \gamma_\Xi P_{\Xi i}$ or $\alpha_\Lambda P_{\Omega i}$, measured by this technique is actually a sum of two components. These components are a term due to the real polarization signal and a "bias" term which is due to uncorrected imperfections in the experimental apparatus or the reconstruction program. Any of these factors which has a non-uniform effect on the $cos\theta_i$ distribution will also increase the overall χ^2 in addition to introducing a bias.

Since the sign of the polarization is defined relative to the production plane, the sign of the polarization is reversed when the production angle is reversed. However, since the biases depend only on the nature of the spectrometer and reconstruction programs, they should not be affected by a change in the production angle. This can be exploited to separate the real polarization from the biases. The measured asymmetries, A_+ and A_- for the positive and negative production angle, can be written in terms of the bias

B, and the real polarization signal P as

$$A_+ = B + P \tag{4.20}$$

$$A_- = B - P \tag{4.21}$$

The bias and real signal components are then extracted from the measured asymmetries:

$$P = \frac{A_+ - A_-}{2} \tag{4.22}$$

$$B = \frac{A_+ + A_-}{2} \tag{4.23}$$

where $P = \alpha_\Lambda \gamma_\Xi P_\Xi$ or $P = \alpha_\Lambda P_\Omega$.

This technique could be used to extract the polarization directly from the reconstructed data sample, without using the hybrid Monte Carlo procedure. However, any biases which do depend on the production angle would be incorporated into the measured asymmetry. In this experiment, there were possible production angle dependent biases that we wished to consider, so the hybrid Monte Carlo technique was used. The major possible source of production angle dependent biases was the spectrometer, since the beam illuminates different parts of the spectrometer at the different production angles.

4.5 Calculation of Target Polarization

Due to the parity conservation argument described in Chapter 1, the only allowed polarization direction is perpendicular to the production plane, which in this experiment is the x direction. The field in the Hyperon magnet precessed this polarization vector into the $x - z$ plane. The polarization at the production target could be extracted by fitting the measured P_x and P_z values to the angle, Φ, through which the parent particle precesses in the hyperon magnet. The precession angle is defined in terms of

known quantities using the expression:

$$\Phi = \left[\frac{\mu}{c} - \frac{q}{mc^2}\right] \int B dl \qquad (4.24)$$

where μ is the known magnetic moment, q is the charge of the hyperon, m is the mass of the hyperon, and $\int B dl$ is the known field integral in the sweeper magnet. For the data taken with a current of -750 Amps in the hyperon magnet, the $\int B dl$ was -17.48 T-m, and for the data with a hyperon magnet current of -2900 Amps, the $\int B dl$ was -24.36 T-m. In the Ξ^- analysis, the current world average magnetic moment value of -0.6507±0.0025 was used [40]. The magnetic moment used in the Ω^- analysis was the value of -2.024±0.056 measured by this experiment [52].

For each data sample, the polarization at the target, P_{tgt}, is calculated by varying P_{tgt} to minimize the χ^2 function:

$$\chi^2 = \sum_i \left[\frac{(P_{xi} - P_{tgt}cos\Phi)^2}{\sigma_{xi}^2} + \frac{(P_{zi} - P_{tgt}sin\Phi)^2}{\sigma_{zi}^2}\right] \qquad (4.25)$$

The subscript i runs over the momentum bins, P_{xi} and P_{zi} are the measured polarization components, and σ_{xi}^2 and σ_{zi}^2 are the uncertainties of the measured polarization components.

The same expression is used in making a magnetic moment measurement, however, in this case the magnetic moment is also treated as a variable parameter.

In this experiment, in the analysis of the Ξ^- data, the value of μ_{Ξ^-} was treated as fixed. For the Ω^- data, the magnetic moment was allowed to vary, so that a measurement of μ_{Ω^-} could be made [52].
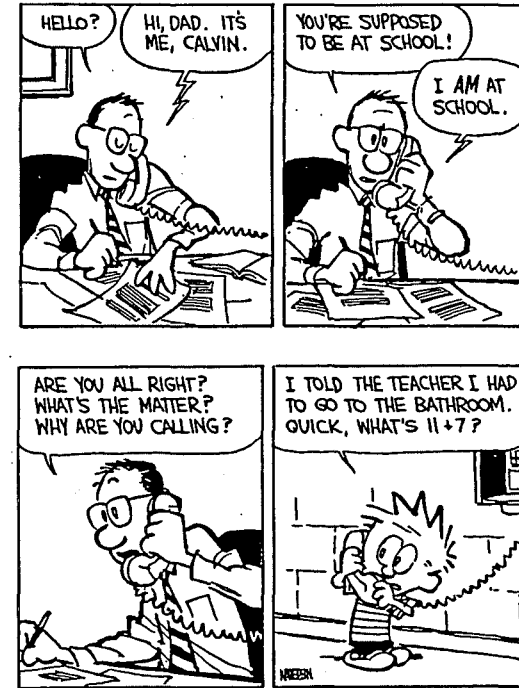
CALVIN AND HOBBES copyright Watterson. Dist. by UNIVERSAL PRESS SYNDICATE. Reprinted with permission. All rights reserved.

Chapter 5

Results and Systematic

Uncertainty Studies

5.1 Polarization Results

All of the unpolarized neutral beam production and polarized neutral beam production data were reconstructed and analyzed for polarization using the methods described in the preceeding chapters.

5.1.1 Unpolarized Neutral Beam Production Data

Table 5.1 gives the measured asymmetries ($\alpha_\Lambda \gamma_\Xi P_\Xi$) and biases as a function of momentum for the Ξ^- unpolarized neutral beam production data for a current of -2900 amps in the hyperon magnet. Table 5.2 gives the measured asymmetries ($\alpha_\Lambda P_\Omega$) and biases for the Ω^- data for this production mode. Figures 5.1 and 5.2 show the unpolarized neutral beam production asymmetries and biases plotted as a function of momentum for both the Ξ^- and Ω^- samples. The momentum averaged asymmetries and biases are given in Table 5.5 for the Ξ^- and Table 5.6 for the Ω^-.

Mom. (GeV/c)	Number of Events (1000s)	View	Asymmetry $\alpha_\Lambda \gamma_\Xi P_\Xi$	Bias
346.	1393	x	-0.0029 ± 0.0016	0.0247 ± 0.0016
		y	0.0000 ± 0.0017	0.0346 ± 0.0017
		z	-0.0038 ± 0.0020	-0.0658 ± 0.0020
369.	1655	x	0.0012 ± 0.0014	-0.0082 ± 0.0014
		y	0.0029 ± 0.0015	0.0224 ± 0.0015
		z	-0.0096 ± 0.0017	-0.0197 ± 0.0017
383.	1793	x	0.0007 ± 0.0013	-0.0029 ± 0.0013
		y	0.0023 ± 0.0014	0.0174 ± 0.0014
		z	-0.0061 ± 0.0016	0.0000 ± 0.0016
399.	1684	x	0.0056 ± 0.0013	-0.0042 ± 0.0013
		y	0.0041 ± 0.0015	0.0153 ± 0.0015
		z	-0.0054 ± 0.0017	0.0096 ± 0.0017
418.	1814	x	0.0033 ± 0.0013	-0.0044 ± 0.0013
		y	0.0023 ± 0.0014	0.0128 ± 0.0014
		z	0.0023 ± 0.0016	0.0095 ± 0.0016
453.	1633	x	0.0005 ± 0.0015	-0.0100 ± 0.0015
		y	-0.0003 ± 0.0015	0.0188 ± 0.0015
		z	0.0005 ± 0.0018	0.0264 ± 0.0018

Table 5.1: Measured Ξ^- asymmetries and biases as a function of momentum for the unpolarized neutral beam production sample with the sweeper magnet set at -2900 amps.

Mom. (GeV/c)	Number of Events (1000s)	View	Asymmetry $\alpha_\Lambda P_\Omega$	Bias
348.	42	x	0.0215 ± 0.0092	-0.0092 ± 0.0092
		y	-0.0005 ± 0.0097	0.0151 ± 0.0097
		z	0.0255 ± 0.0115	0.0208 ± 0.0115
380.	42	x	0.0048 ± 0.0084	0.0086 ± 0.0084
		y	0.0125 ± 0.0094	0.0363 ± 0.0094
		z	0.0204 ± 0.0101	0.0394 ± 0.0101
403.	37	x	0.0207 ± 0.0090	-0.0006 ± 0.0090
		y	0.0117 ± 0.0099	-0.0042 ± 0.0099
		z	0.0311 ± 0.0103	0.0524 ± 0.0311
443.	44	x	0.0272 ± 0.0086	0.0150 ± 0.0086
		y	0.0065 ± 0.0090	0.0088 ± 0.0090
		z	0.0149 ± 0.0100	0.0766 ± 0.0100

Table 5.2: Measured Ω^- asymmetries and biases as a function of momentum for the unpolarized neutral beam production sample with the sweeper magnet set at -2900 amps.
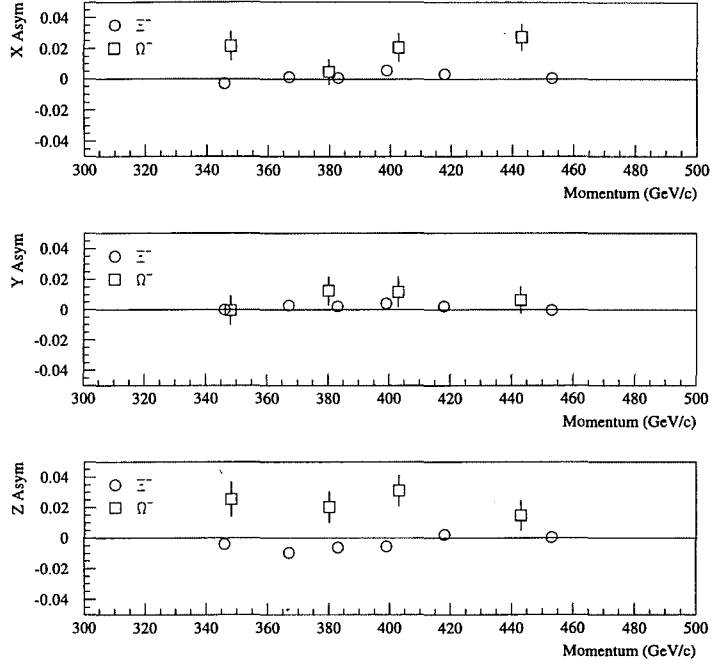
Figure 5.1: Asymmetries ($\alpha_\Lambda \gamma_\Xi P_\Xi$ and $\alpha_\Lambda P_\Omega$) for the unpolarized neutral beam production sample with the sweeper magnet set at −2900 Amps.

Figure 5.2: Biases for the unpolarized neutral beam production sample with the sweeper magnet set at −2900 Amps.

Mom. (GeV/c)	Number of Events (1000s)	View	Asymmetry $\alpha_\Lambda\gamma_\Xi P_\Xi$	Bias
259.	731	x	−0.0063±0.0022	−0.0500±0.0022
		y	0.0021±0.0024	0.0374±0.0024
		z	−0.0041±0.0031	−0.0766±0.0031
282.	813	x	−0.0032±0.0019	−0.0053±0.0019
		y	0.0066±0.0022	0.0235±0.0022
		z	−0.0064±0.0025	−0.0446±0.0064
299.	827	x	−0.0070±0.0019	−0.0002±0.0019
		y	0.0032±0.0022	0.0180±0.0022
		z	−0.0055±0.0023	−0.0258±0.0023
318.	745	x	−0.0050±0.0021	−0.080±0.0021
		y	0.0023±0.0023	0.0255±0.0023
		z	0.0000±0.0025	−0.0049±0.0025
349.	645	x	−0.0084±0.0023	−0.0294±0.0023
		y	0.0014±0.0025	0.0303±0.0025
		z	0.0069±0.0028	0.0269±0.0028

Table 5.3: Measured Ξ^- asymmetries and biases as a function of momentum for the unpolarized neutral beam production sample with the sweeper magnet set at −750 amps.

Table 5.3 gives the measured asymmetries ($\alpha_\Lambda\gamma_\Xi P_\Xi$) and biases as a function of momentum for the unpolarized neutral beam production data for a current of −750 amps in the hyperon magnet. Table 5.4 gives the same results for the Ω^-s in this data sample. Figures 5.3 and 5.4 show the asymmetries and biases of this sample plotted as a function of momentum. The momentum averaged asymmetries and biases are given in Table 5.5 for the Ξ^- and Table 5.6 for the Ω^-.

In this experiment, the only parity conserving direction for the polarization at the second target was $\hat{x}$. The hyperon magnet precessed this polarization vector into the $\hat{x} - \hat{z}$ plane. Therefore, any polarization would be indicated by measured non-zero asymmetries in the $\hat{x}$ and $\hat{z}$-directions. The precession angle depends only on the magnetic moment of the particle and the magnetic field through which the particle passes. The precession angle should be momentum independent. From Tables 5.1 and 5.3 and Figures 5.1 and 5.3 it can be seen that there is no clear polarization signal for the

Mom. (GeV/c)	Number of Events (1000s)	View	Asymmetry $\alpha_\Lambda P_\Omega$	Bias
260.	10	x	0.0140±0.0202	−0.0232±0.0202
		y	−0.0013±0.0216	0.0446±0.0216
		z	0.0166±0.0314	−0.1401±0.0314
288.	15	x	0.0434±0.0144	−0.0002±0.0144
		y	0.0203±0.0172	0.0425±0.0172
		z	0.0102±0.0208	−0.0104±0.0208
312.	13	x	0.0235±0.0157	−0.0144±0.0157
		y	−0.0094±0.0185	−0.0066±0.0185
		z	0.0187±0.0199	−0.0029±0.0199
349.	13	x	−0.0163±0.0171	0.0154±0.0171
		y	0.0163±0.0180	0.0250±0.0180
		z	0.0117±0.0188	0.0636±0.0188

Table 5.4: Measured Ω^- asymmetries and biases as a function of momentum for the unpolarized neutral beam production sample with the sweeper magnet set at −750 amps.
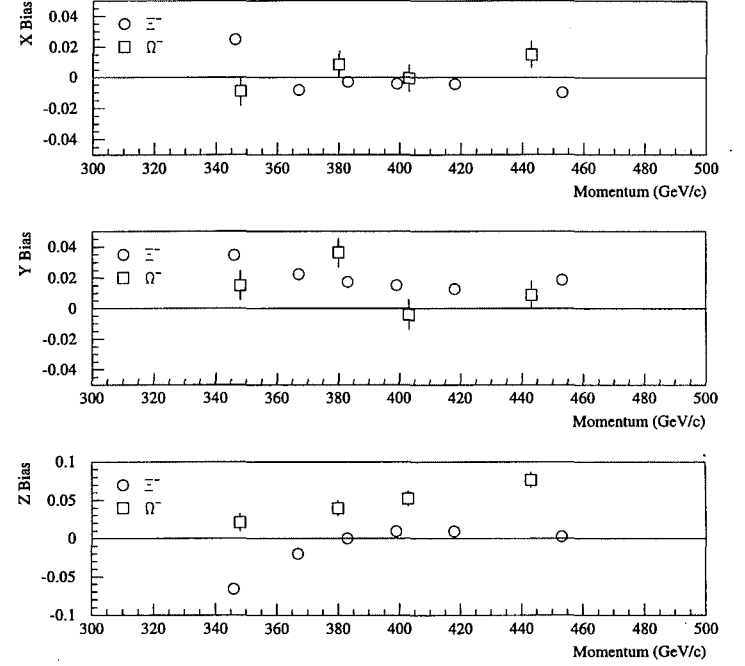
Sweeper Current	Mom. (GeV/c)	Number of Events (1000s)	View	Asymmetry $\alpha_\Lambda\gamma_\Xi P_\Xi$	Bias
750 Amps	300.	3768	x	−0.0062±0.0009	−0.0165±0.0009
			y	0.0032±0.0010	0.0263±0.0010
			z	−0.0027±0.0012	−0.0236±0.0012
2900 Amps	395.	9971	x	0.0019±0.0006	−0.0018±0.0006
			y	0.0019±0.0006	0.0195±0.0006
			z	−0.0040±0.0007	−0.0045±0.0007

Table 5.5: Overall unpolarized neutral beam production Ξ^- sample asymmetries and biases for the two sweeper magnet settings.

Sweeper Current	Mom. (GeV/c)	Number of Events (1000s)	View	Asymmetry $\alpha_\Lambda P_\Omega$	Bias
750 Amps	304.	50	x	0.0186±0.0083	−0.0032±0.0083
			y	0.0072±0.0093	0.0263±0.0093
			z	0.0140±0.0109	−0.0010±0.0109
2900 Amps	394.	167	x	0.0179±0.0044	0.0044±0.0044
			y	0.0073±0.0048	0.0141±0.0048
			z	0.0218±0.0053	0.0496±0.0053

Table 5.6: Overall unpolarized neutral beam production Ω^- sample asymmetries and biases for the two sweeper magnet settings.
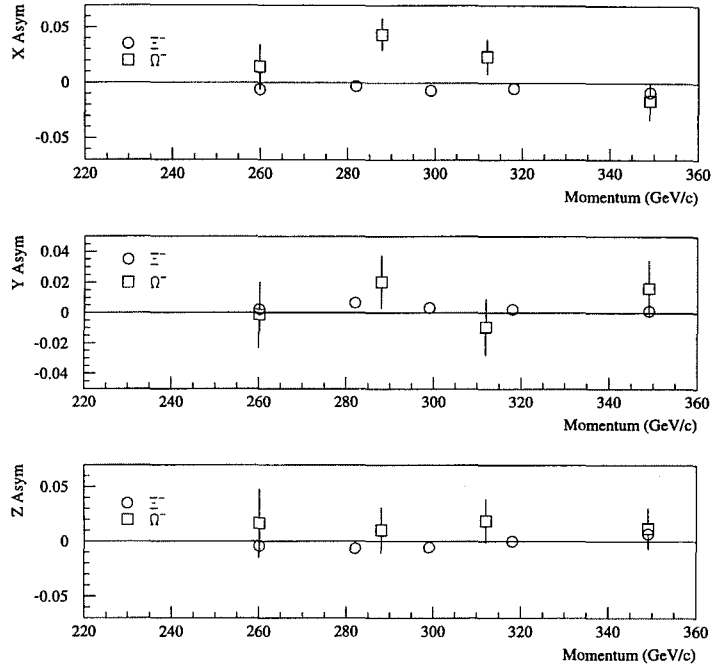
Figure 5.3: Asymmetries $(\alpha_\Lambda \gamma_\xi P_\Xi$ and $\alpha_\Lambda P_\Omega)$ for the unpolarized neutral beam production sample with the sweeper magnet set at -750 Amps.
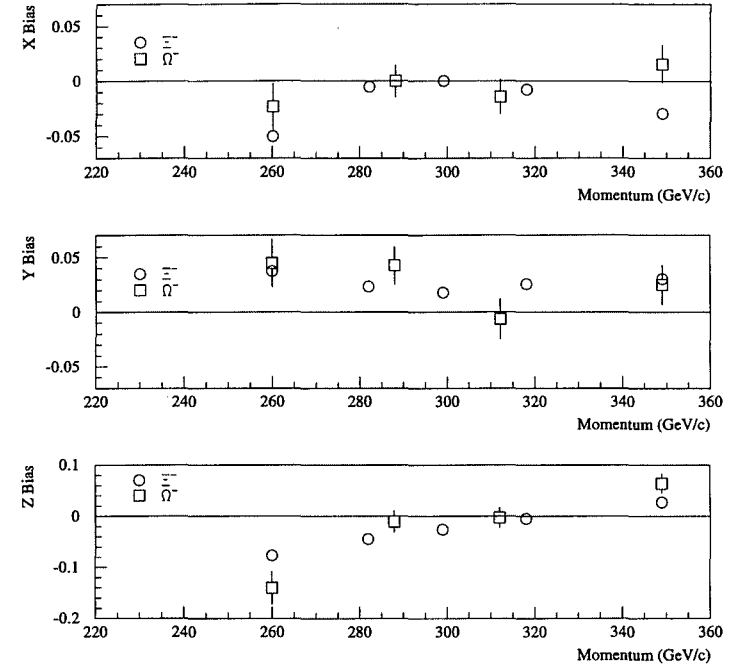
Figure 5.4: Biases for the unpolarized neutral beam production sample with the sweeper magnet set at -750 Amps.

Ξ^- data. Figure 5.5 shows this more clearly. This figure shows the Ξ^- and Ω^- precession angle, $\Phi = \arctan(P_z/P_x)$, for the various momentum bins for the -2900 amp data. The expected precession angles, calculated using the known magnetic moments, are also shown. All the Ω^- points are consistent with the expected precession angle, indicating a $\hat{x}$ polarization at the target being precessed into the $\hat{x}$ - $\hat{z}$-plane. The Ξ^- sample does not show a similar consistency. This indicates that the Ξ^- sample was not polarized.

5.1.2 Polarized Neutral Beam Production Data

Table 5.7 gives the measured asymmetries ($\alpha_\Lambda \gamma_\Xi P_\Xi$) and biases as a function of momentum for the polarized neutral beam Ξ^- data. Table 5.8 gives the measured asymmetries and biases for the Ω^-s produced using the polarized neutral beam technique. Figures 5.6 and 5.7 show the measured asymmetries and biases plotted as a function of momentum for the Ξ^- and Ω^- data. The momentum averaged asymmetries and biases are given in Table 5.9 for the Ξ^- and Table 5.10 for the Ω^-.

Figure 5.8 shows the measured precession angles for the Ξ^- and Ω^- events in this data sample. These figures show that measured precession angles agree with the expected value, indicating that both the Ξ^- and Ω^- samples are polarized.

The polarization at the production target was extracted by fitting to a single magnetic moment using the method described in section 4.5. The target polarizations for the different samples are given in Table 5.11 and are plotted in Figure 5.9.

5.1.3 Discussion of Biases

Figure 5.10 shows the Ξ^- biases for the two unpolarized neutral beam data samples and the polarized neutral beam sample. This figure shows that biases for the polarized neutral beam sample and the unpolarized neutral beam sample with a current of -2900
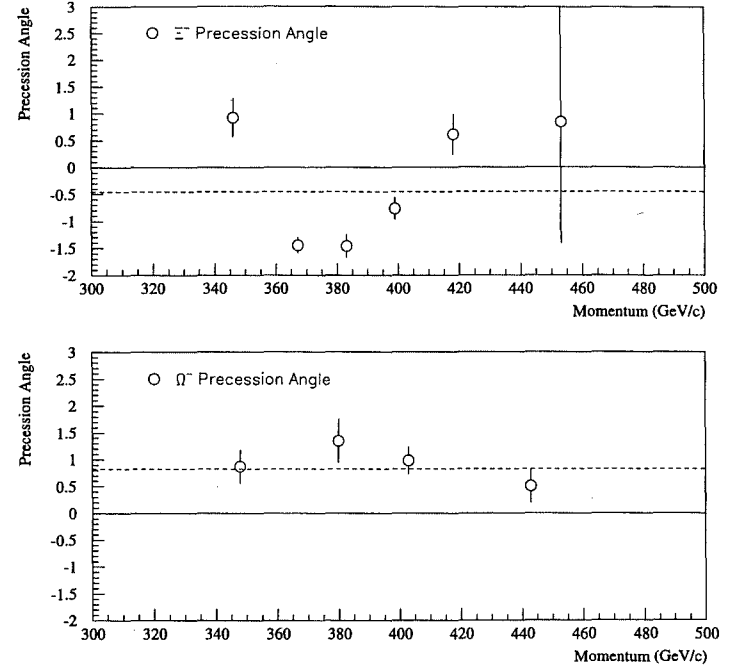

Figure 5.5: Measured precession angles for the unpolarized neutral beam production sample with the sweeper magnet set at -2900 Amps. The dashed lines show the expected precession angles calculated using the known magnetic moments.

Mom. (GeV/c)	Number of Events (1000s)	View	Asymmetry $\alpha_\Lambda \gamma_\Xi P_\Xi$	Bias
347.	93	x	−0.0395±0.0061	0.0126±0.0061
		y	−0.0149±0.0068	0.0496±0.0068
		z	0.0168±0.0078	−0.0849±0.0078
367.	125	x	−0.0526±0.0049	−0.0036±0.0049
		y	0.0006±0.0057	0.0297±0.0057
		z	0.0261±0.0062	−0.0117±0.0062
383.	138	x	−0.0671±0.0046	−0.0121±0.0046
		y	0.0030±0.0054	0.0102±0.0054
		z	0.0306±0.0059	−0.0089±0.0059
399.	129	x	−0.0557±0.0048	−0.0050±0.0048
		y	0.0092±0.0056	0.0035±0.0056
		z	0.0232±0.0062	0.0086±0.0062
417.	130	x	−0.0695±0.0048	−0.0136±0.0048
		y	−0.0024±0.0056	0.0002±0.0056
		z	0.0352±0.0062	0.0125±0.0062
451.	96	x	−0.0797±0.0060	−0.0186±0.0060
		y	−0.0025±0.0065	0.0153±0.0065
		z	0.0592±0.0075	0.0377±0.0075

Table 5.7: Measured Ξ^- asymmetries and biases as a function of momentum for the polarized neutral beam production sample.

Mom. (GeV/c)	Number of Events (1000s)	View	Asymmetry $\alpha_\Lambda P_\Omega$	Bias
351.	5	x	−0.0351±0.0277	−0.0338±0.0277
		y	0.0207±0.0295	0.0699±0.0295
		z	−0.0596±0.0354	0.0212±0.0354
380.	5	x	−0.0100±0.0242	0.0215±0.0242
		y	−0.0299±0.0276	0.0218±0.0276
		z	0.0103±0.0290	0.0516±0.0290
403.	4	x	−0.0146±0.0261	0.0196±0.0261
		y	−0.0022±0.0290	−0.0648±0.0290
		z	−0.0807±0.0309	0.0386±0.0309
439.	4	x	−0.0678±0.0273	0.0079±0.0273
		y	0.0312±0.0285	−0.0677±0.0285
		z	−0.0082±0.0314	0.0517±0.0314

Table 5.8: Measured Ω^- asymmetries and biases as a function of momentum for the polarized neutral beam production sample.

Sweeper Current	Mom. (GeV/c)	Number of Events (1000s)	View	Asymmetry $\alpha_\Lambda \gamma_\Xi P_\Xi$	Bias
2900 Amps	393.	711	x	−0.0605±0.0021	−0.0072±0.0021
			y	−0.0004±0.0024	0.0165±0.0024
			z	0.0300±0.0027	−0.0071±0.0027

Table 5.9: Overall Ξ^- sample asymmetries and biases for the polarized neutral beam production sample.

Sweeper Current	Mom. (GeV/c)	Number of Events (1000s)	View	Asymmetry $\alpha_\Lambda P_\Omega$	Bias
2900 Amps	393.	18	x	−0.0283±0.0132	0.0096±0.0132
			y	0.0066±0.0144	−0.0084±0.0144
			z	−0.0341±0.0159	0.0428±0.0159

Table 5.10: Overall Ω^- sample asymmetries and biases for the polarized neutral beam production sample.

Neutral Beam Type	Sweeper Current	Particle	Number of Events (1000s)	Mom. (GeV/c)	Polarization
Polarized	−2900 Amps	Ξ^-	711	393.	−0.118±0.004
		Ω^-	18	393.	−0.069±0.023
Unpolarized	−750 Amps	Ξ^-	3768	300.	−0.006±0.001
		Ω^-	50	304.	+0.036±0.015
	−2900 Amps	Ξ^-	9971	395.	−0.003±0.001
		Ω^-	167	394.	+0.044±0.008

Table 5.11: Fitted target polarizations for all data samples.
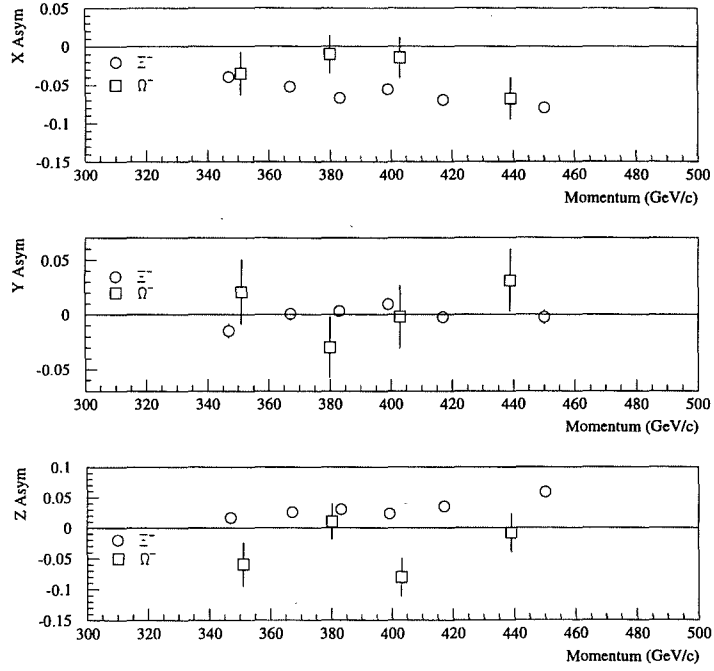
Figure 5.6: Asymmetries ($\alpha_\Lambda \gamma_\Xi P_\Xi$ and $\alpha_\Lambda P_\Omega$) for the polarized neutral beam production sample.
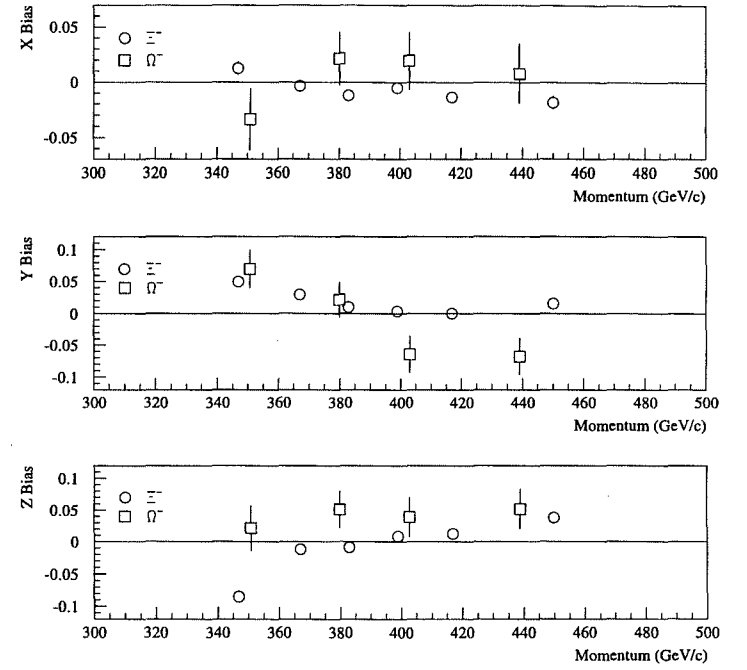

Figure 5.7: Biases for the polarized neutral beam production sample.
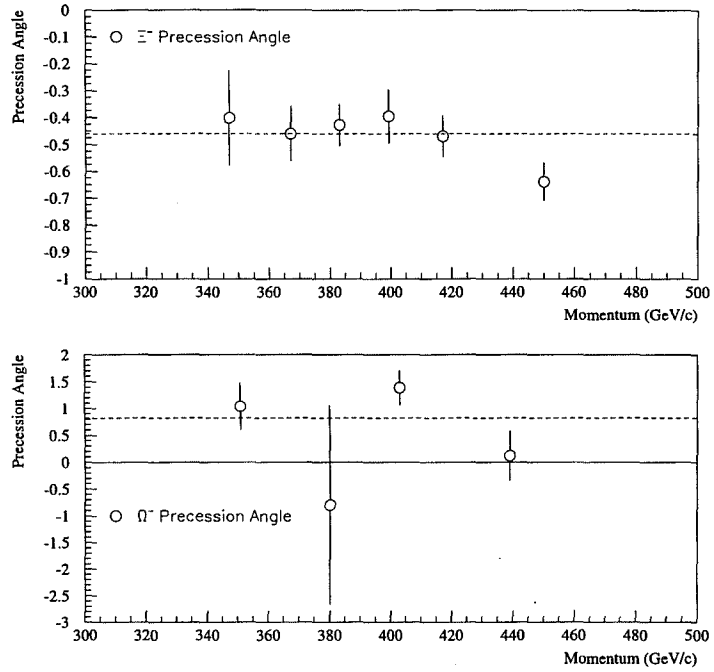
Figure 5.8: Measured precession angles for the polarized neutral beam production sample. The dashed lines show the expected precession angles calculated using the known magnetic moments.
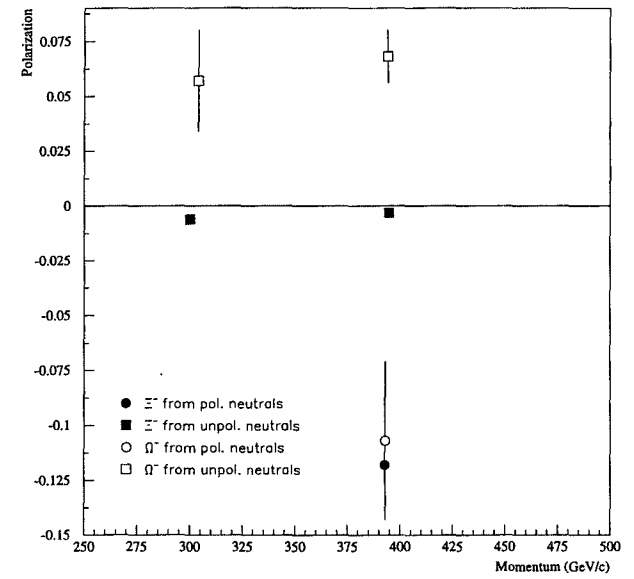
Figure 5.9: Fitted target polarizations for all samples.

amps in the Hyperon magnet are consistent with each other. This is expected since both samples cover the same momentum region. Also, it can be seen that, with the exception of the the lowest momentum point in the x view for the 750 amp sample, the biases for the two unpolarized neutral beam samples show a similar behavior, as expected. The biases for these two samples are not the same in the momentum region where they overlap. This is due to the fact that while the data from the two samples have the same momentum, the particles in the two samples pass through different regions of the charged collimator and the spectrometer.

The biases for the Ξ^- and Ω^- samples can be compared in Figures 5.2, 5.4, and 5.7. These figures show that while the Ξ^- and Ω^- biases have similar momentum dependences, their magnitudes are different. This difference is due to the different parent and daughter particle masses. Due to these mass differences, the daughter particles from the two decays have a different range of allowed opening angles in the laboratory. This means that the daughter particles from the two decays will have different distributions in the various parts of the spectrometer.

The large magnitude of the biases, especially in the low momentum region of the x-view caused some concern. It was found that the data selection criteria could be varied to reduce these biases. However, reducing the biases had no effect on the asymmetry results.

Monte Carlo studies were performed using both polarized and unpolarized Monte Carlo data, and it was found the biases observed in the Monte Carlo analysis were in general similar to those of real data. In addition, the asymmetry results for the unpolarized Monte Carlo data adequately matched the asymmetry results of the unpolarized neutral beam data sample. The results of the asymmetry analysis of the polarized Monte Carlo data were consistent with the input polarization used in the generation of the Monte Carlo data.

Figure 5.10: Comparision of biases for all the Ξ^- samples.

5.2 Systematic Studies

5.2.1 Single-track Triggers

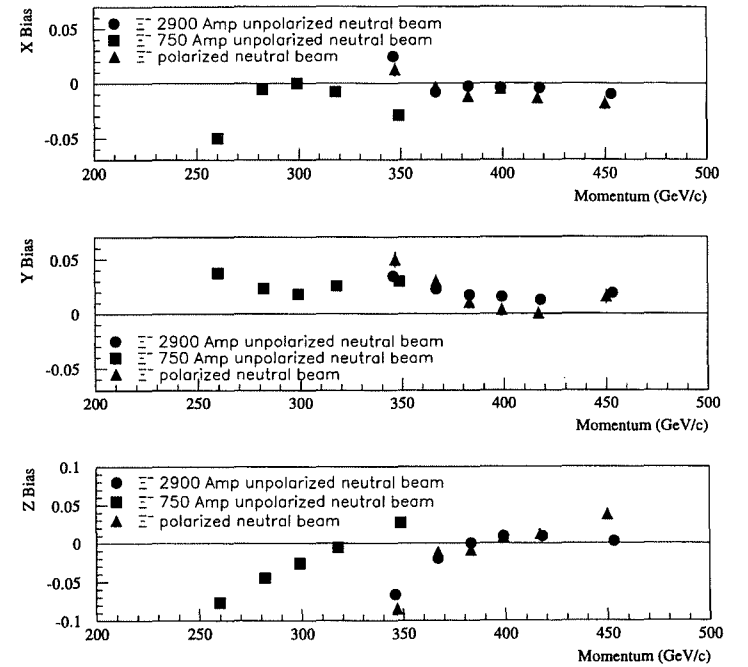The effect of requiring hits in C11 and C12 in the trigger was studied by analyzing Ξ^- events that were only required to have hits in the scintillation counters S1 and S2 with no hits in V1 or V2. This trigger selected events that were from charged particles that had entered the spectrometer from the Hyperon magnet and were not part of a shower from an upstream interaction. Table 5.12 gives the measured asymmetries $(\alpha_\Lambda \gamma_\Xi P_\Xi)$ and biases as a function of momentum for Ξ^- events selected by the single-track trigger. These events are from the unpolarized neutral beam production data sample taken with a current of -2900 amps in the Hyperon magnet.

Figures 5.11 and 5.12 show the unpolarized neutral beam production asymmetries and biases plotted as a function of momentum for the Ξ^- events selected by the single-track trigger. The distributions for events from the general unpolarized neutral beam production sample are shown for comparison. All of these distributions agree within the statistical errors of the measurements. As a further test, the mass, momentum, Ξ^- and Λ vertex, target position, χ^2_G/DF and χ^2_Λ distributions of the events selected by the single-track trigger were compared to the distributions for events selected by the three-track trigger, and no significant differences were found.

5.2.2 Data at 0 mrad production angle.

Table 5.13 gives the measured asymmetries $(\alpha_\Lambda \gamma_\Xi P_\Xi)$ and biases as a function of momentum for data produced with no production angle. This data was collected with two different magnetic field polarities in the neutral sweeper magnet and this division of the sample was used in the bias cancellation instead of a positive and negative production angle division. Figures 5.13 and 5.14 show the Ξ^- asymmetries and biases plotted as a function of momentum for the 0 mrad production angle data.

Mom. (GeV/c)	Number of Events (1000s)	View	Asymmetry $\alpha_\Lambda \gamma_\Xi P_\Xi$	Bias
346.	19	x	-0.0148 ± 0.0134	-0.0405 ± 0.0134
		y	0.0148 ± 0.0143	0.0097 ± 0.0143
		z	-0.0170 ± 0.0169	-0.0316 ± 0.0169
367.	22	x	-0.0013 ± 0.0115	-0.0283 ± 0.0115
		y	-0.0119 ± 0.0129	0.0175 ± 0.0129
		z	-0.0080 ± 0.0141	-0.0253 ± 0.0141
383.	25	x	-0.0093 ± 0.0110	0.0119 ± 0.0110
		y	0.0019 ± 0.0121	0.0204 ± 0.0121
		z	-0.0348 ± 0.0136	0.0083 ± 0.0136
399.	24	x	0.0066 ± 0.0114	0.0130 ± 0.0114
		y	-0.0023 ± 0.0125	-0.0077 ± 0.0125
		z	-0.0152 ± 0.0142	0.0107 ± 0.0142
418.	26	x	0.0279 ± 0.0108	0.0063 ± 0.0108
		y	0.0144 ± 0.0118	0.0031 ± 0.0118
		z	0.0167 ± 0.0135	-0.0115 ± 0.0135
456.	25	x	0.0086 ± 0.0118	-0.0352 ± 0.0118
		y	0.0037 ± 0.0122	0.0092 ± 0.0122
		z	0.0083 ± 0.0145	0.0297 ± 0.0145

Table 5.12: Measured Ξ^- asymmetries and biases as a function of momentum for the single-track unpolarized neutral beam production sample with the sweeper magnet set at -2900 amps.
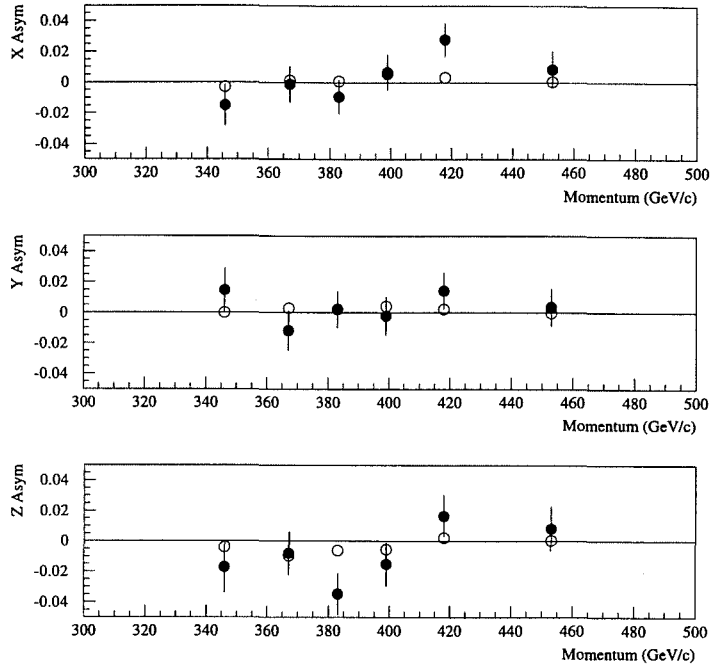
Figure 5.11: Comparison of Ξ^- asymmetries $(\alpha_\Lambda \gamma_\Xi P_\Xi)$ for the normal trigger (open circles) and single-track trigger (filled circles).
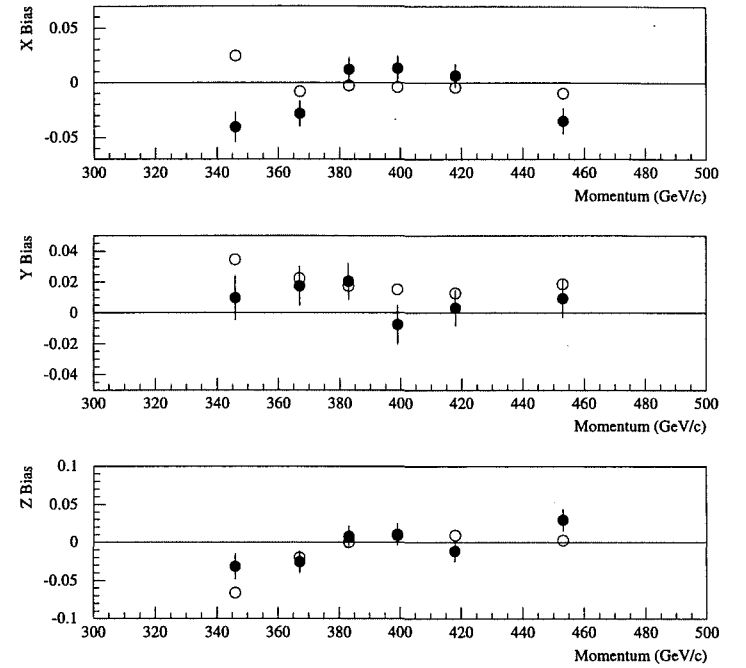
Figure 5.12: Comparison of Ξ^- biases for the normal trigger (open circles) and single-track trigger (filled circles).

Mom. (GeV/c)	Number of Events (1000s)	View	Asymmetry $\alpha_\Lambda\gamma_\Xi P_\Xi$	Bias
347.	124	x	−0.0018±0.0053	0.0282±0.0053
		y	0.0103±0.0056	0.0472±0.0056
		z	0.0072±0.0067	−0.0816±0.0067
367.	172	x	−0.0102±0.0042	−0.0035±0.0042
		y	0.0014±0.0047	0.0258±0.0047
		z	0.0041±0.0052	−0.0235±0.0052
383.	206	x	0.0006±0.0038	0.0028±0.0038
		y	0.0020±0.0042	0.0140±0.0042
		z	0.0089±0.0048	0.0013±0.0048
399.	209	x	−0.0021±0.0038	−0.0058±0.0038
		y	−0.0012±0.0042	0.0124±0.0042
		z	0.0049±0.0048	0.0068±0.0048
418.	243	x	−0.0010±0.0036	0.0003±0.0036
		y	0.0030±0.0038	0.0080±0.0038
		z	0.0037±0.0044	0.0055±0.0044
455.	245	x	−0.0005±0.0038	−0.0052±0.0038
		y	0.0014±0.0039	0.0083±0.0039
		z	0.0070±0.0047	0.0241±0.0047

Table 5.13: Measured Ξ^- asymmetries and biases as a function of momentum for data with no production angle.

To study how well the polarization analysis measured unpolarized data samples, Monte Carlo Ξ^- data generated with no polarization was analyzed. Figure 5.15 shows the results of this analysis, with the measured asymmetries for the unpolarized neutral beam production data for comparison. This figure shows that the measured asymmetries for the Monte Carlo data are consistent with no polarization. The agreement between the real data and Monte Carlo asymmetries also add support to our conclusion that the Ξ^-s produced by the unpolarized neutral beam are unpolarized.

5.2.3 Other Systematic Studies

To search for possible time dependent effects in the data, the unpolarized neutral beam production Ξ^- data sample with sweeper current set at −2900 amps was broken into

Figure 5.13: Comparison of Ξ^- asymmetries ($\alpha_\Lambda\gamma_\Xi P_\Xi$) for the unpolarized neutral beam production data (open circles) and 0 mrad production data (filled circles).

Figure 5.14: Comparison of Ξ^- biases for the unpolarized neutral beam production data (open circles) and 0 mrad production data (filled circles).
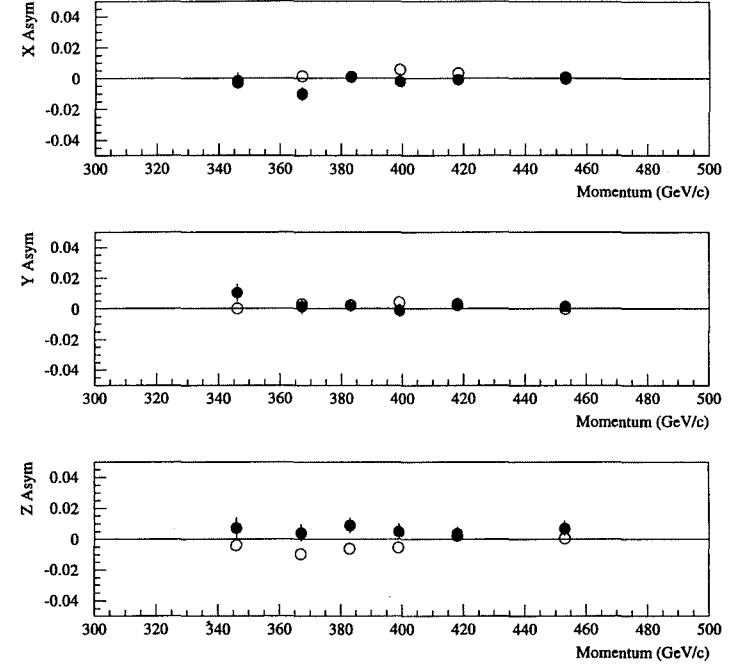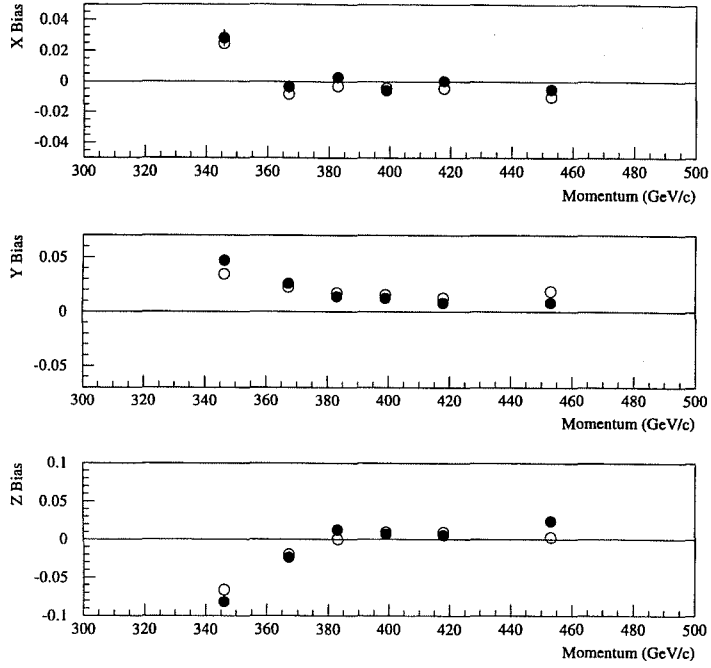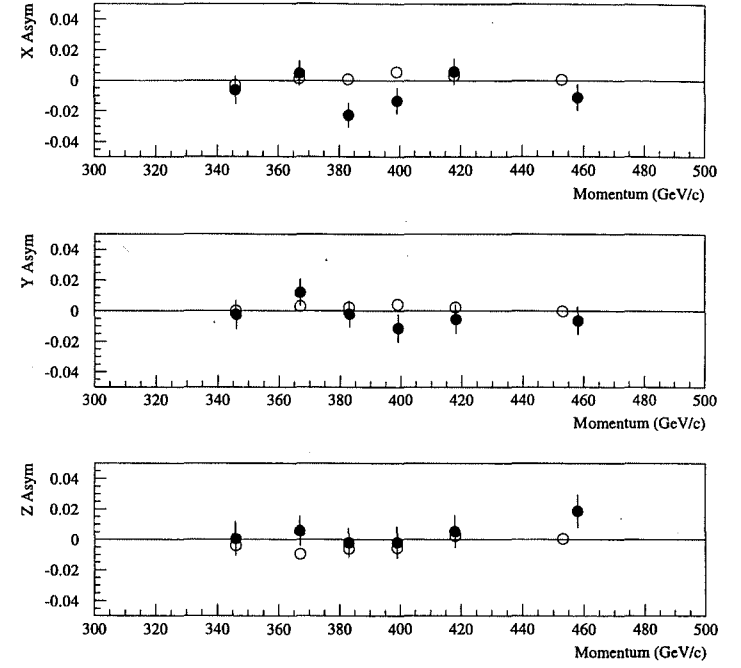

Figure 5.15: Comparison of Ξ^- asymmetries ($\alpha_\Lambda \gamma_\Xi P_\Xi$) for the unpolarized neutral beam production data (open circles) and unpolarized Monte Carlo data (filled circles).

Normal Criteria	"Tighter" Criteria
$\Delta m_{\Xi^-} < 15 MeV/c$	$\Delta m_{\Xi^-} < 8 MeV/c$
$\chi^2{}_G/DF < 4$	$\chi^2{}_G/DF < 3$
$\chi^2{}_\Lambda < 15$	$\chi^2{}_\Lambda < 10$
$\|X_T\| < 0.9 cm$	$\|X_T\| < 0.5 cm$
$\|Y_T\| < 0.8 cm$	$\|Y_T\| < 0.5 cm$
maximum $Z_{\Xi^-} = 2500$ cm	maximum $Z_{\Xi^-} = 2000$ cm
minimum $Z_{\Xi^-} = -1000$ cm	minimum $Z_{\Xi^-} = +200$ cm

Table 5.14: Normal and "tighter" data selection criteria.

seven smaller parts. The subdivision was based on the point in the run the data were taken. Figures 5.16 and 5.17 show the measured asymmetries and biases for the seven subsamples. There is no evidence of a time dependent systematic effect.

As a final systematic study, the effect of variations in the data selection criteria were studied. This was done by studying the effect of tighter selection criteria on the Ξ^- magnetic moment measured for the polarized neutral beam data sample. Table 5.14 shows the normal and tighter data selection criteria that were used in this study. The effects of varying each selection criteria were studied individually. Figure 5.18 shows the measured Ξ^- magnetic moment as a function of momentum for the different selection criteria. The shaded region represents the world average measurement of μ_{Ξ^-} and its measured error [40]. There is no evidence of any systematic effect due to the data selection method.

5.3   Summary of Results

To summarize, the polarization of Ξ^-s and Ω^- produced by an unpolarized neutral beam has been has been measured for the first time. The Ξ^-s were found to be unpolarized. The observed Ω^- polarization was $+0.044 \pm 0.008$ at an average momentum of 394. GeV/c and $+0.036 \pm 0.015$ at an average momentum of 305. GeV/c.

The polarization of Ξ^-s and Ω^-s produced by a polarized neutral beam was also
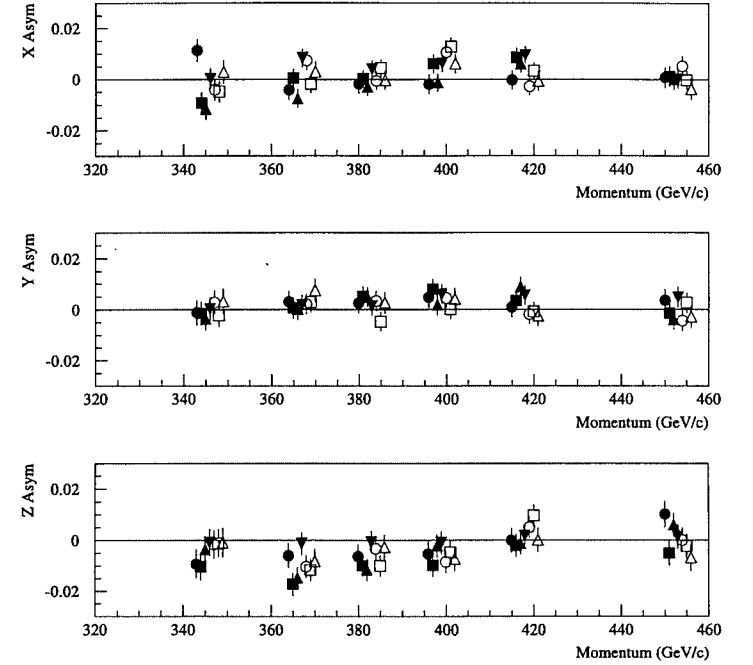
Figure 5.16: Ξ^- asymmetries ($\alpha_\Lambda \gamma_\Xi P_\Xi$) for seven unpolarized neutral beam production data subsamples.
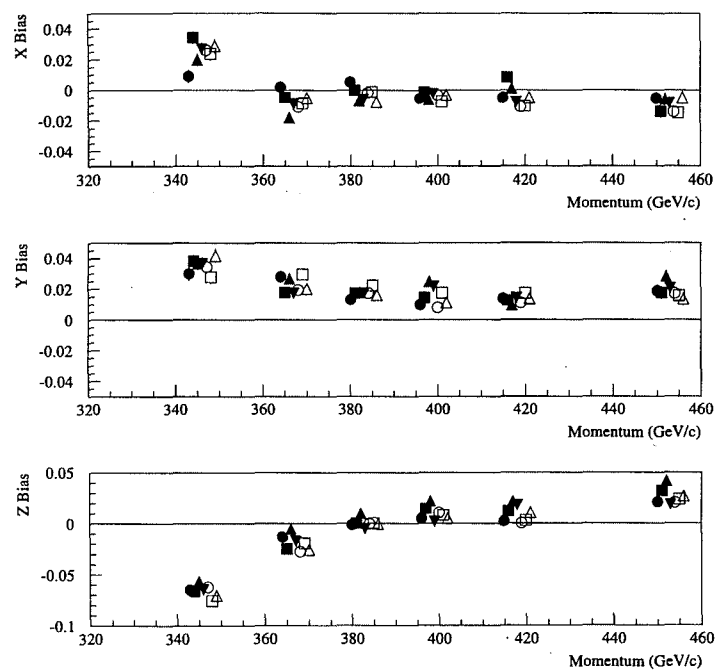
Figure 5.17: Ξ^- biases for seven unpolarized neutral beam production data subsamples.
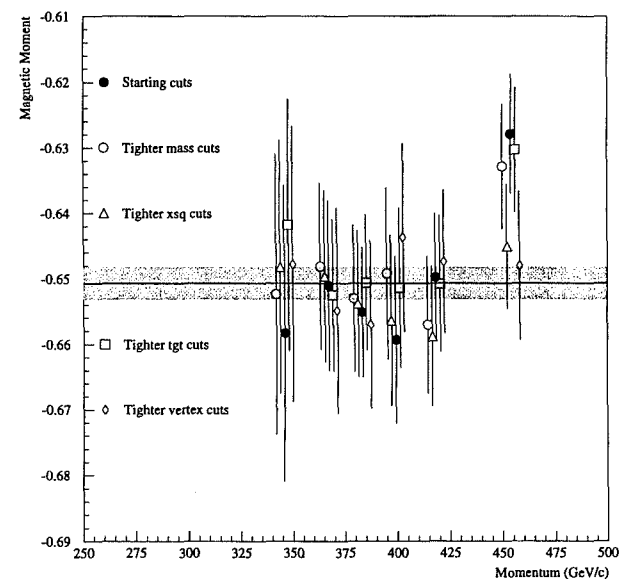
Figure 5.18: Measured Ξ^- magnetic moment for various "tighter" data selection criteria.

studied. The Ξ^- sample had a polarization of -0.118 ± 0.004 at an average momentum of 393. GeV/c. The Ω^- sample had a polarization of -0.069 ± 0.023 at an average momentum of 394. GeV/c.
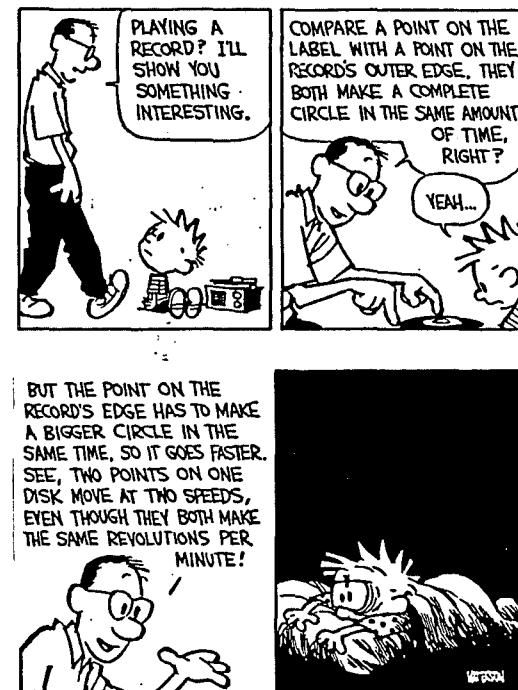
Chapter 6

Conclusions

6.1 Comparision With Previous Measurements

The measured Ξ^- and Ω^- polarizations at the production target are show in Figures 6.1 and 6.2 for both the polarized and unpolarized neutral beam production modes. Results for a previous measurement using the polarized neutral beam production mode are shown for comparison [26]. These figures show that the polarized neutral beam production mode results discussed in this thesis are consistent with the previous measurement.

6.2 Theoretical Predictions

Of the models discussed in Chapter 1, only two are able to make predictions of the polarizations that were studied in this experiment. The Lund model of Andersson, Gustafson, and Ingelman[33] predicts that all s quarks produced from the sea should be polarized in the negative direction. With this prediction for the s quark polarization, one expects that Ω^-s produced from an unpolarized neutral beam would be polarized with a negative sign. This does not agree with the experimental observation of a positive
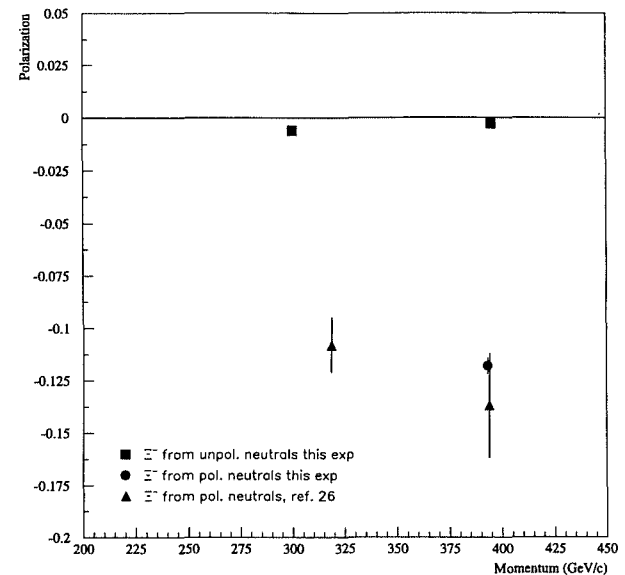
Figure 6.1: Comparision of Ξ^- polarization results.
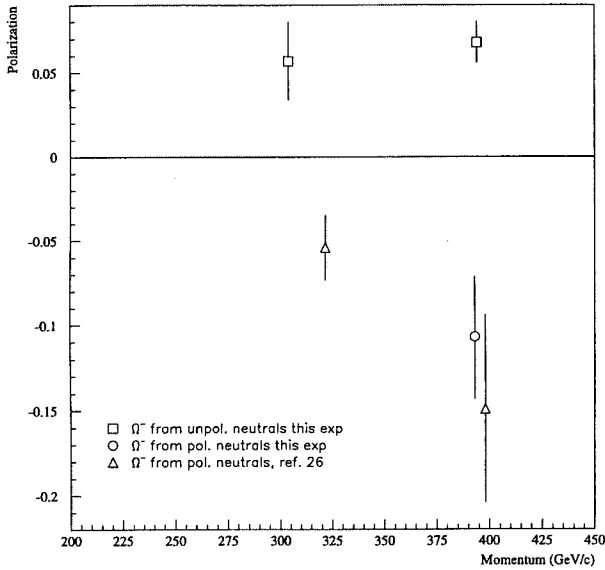
Figure 6.2: Comparision of Ω^- polarization results.

polarization.

The model of DeGrand and Miettinen [29] makes more detailed predictions of the polarization of hyperons produced from both a polarized and an unpolarized neutral beam. The predictions of this model with the modification introduced by Bonner *et al.* [21] to allow for quark spin flips are given in Table 1.3.

For production from the unpolarized neutral beam, we set the incident beam polarization, $d = 0$. To simplify the calculations, any differences between ϵ and ϵ' and δ and δ' are neglected, and we set $\delta \approx \epsilon$. In the development of their model, DeGrand and Miettinen [29] do not make a distinction between δ and δ' or ϵ and ϵ'. In addition, they also assume $\delta \approx \epsilon$. In making a fit to experimental data, Kroll finds that δ and ϵ are not approximately equal, and that the primed and unprimed parameters are not similar [31]. In addition, it should be noted that since hyperon polarization is momentum dependent, these parameters are also momentum dependent. Differences of 10% between the values of δ and ϵ do not have a significant effect on any of the Ξ^- predictions. For the Ω^- predictions, the difference between δ and ϵ is significant. Table 1.3 shows that for Ω^- production from Λ^0s and Ξ^0s, there are terms involving $\delta - \epsilon$. For ϵ fixed at a value of 0.1, and δ varied between 0.9ϵ and 1.1ϵ, the predicted polarization for Ω^-s produced from Λ^0s varies from -0.008 to $+0.008$. The prediction for production from Ξ^0s varies from -0.013 to $+0.003$. Note that in both cases the magnitude of the predicted polarization is small.

The values used for the spin flip parameters are: $\tau_1 = 0.2$ and $\tau_2 = 0.4$. This extension to the model has a significant effect on several of the predictions. The values used for τ_1 and τ_2 come from experimental data [21], and the predictions are not sensitive to small variations in the values used for these parameters. The predicted polarizations for the different components of the neutral beam are given in Table 6.1. In this model, $-\epsilon$ is the prediction for the polarization of Λ^0 produced from protons, and a value of $\epsilon = 0.1$ is used.

Interaction	Predicted Polarization	Value for $\epsilon = 0.1$	Value with no spin flip
$n \to \Xi^-$	$-\epsilon$	-0.1	-0.1
$\Lambda^0 \to \Xi^-$	-0.08ϵ	-0.009	-0.017
$\Xi^0 \to \Xi^-$	$+0.8\epsilon$	$+0.083$	$+0.1$
$n \to \Omega^-$	0	0	0
$\Lambda^0 \to \Omega^-$	$\frac{5}{6}(\epsilon - \delta)$	$-0.008 - +0.008$	
$\Xi^0 \to \Omega^-$	$\frac{10(\delta-\epsilon)-0.8\epsilon}{17.6}$	$-0.013 - +0.003$	

Table 6.1: Predicted polarizations for production from an unpolarized neutral beam. See the text for details about the Ω^- predictions.

The composition of our neutral beam and the cross sections for Ξ^- and Ω^- production have not been measured, so combining these predictions is difficult. An attempt at estimating the sources of the final state $\Xi-$s and Ω^-s has been made based on measurements of neutron, Λ^0 and Ξ^0 production cross sections [25]. Diehl assumed that the cross sections for Ξ^- and Ω^- production by the components of the neutral beam were similar to other process with similar quark exchanges. This calculation predicted that Ξ^-s were mostly produced by Λ^0s followed by Ξ^0s, and that Ω^-s were produced by Ξ^0s followed by Λ^0s, with neutron production playing a small role in both cases.

For the Ξ^-, the predicted polarization is small for Λ^0 production which is thought to be the dominant production mechanism. The predictions for neutron and Ξ^0 production are larger and have similar magnitudes, but opposite signs. With the estimates discussed above for the contributions of the various components of the neutral beam, a small negative polarization could be expected. Zero final state polarization is also possible with an appropriate combination of contributions from the various components of the neutral beam. Experimentally, no final state polarization is observed.

For Ω^- production, the magnitude of the predicted polarization is small for all of the production mechanisms, and the signs of the polarization depends on the parameters in the models. The measured values of $+0.044\pm0.008$ and $+0.036\pm0.015$, are larger than all of the predictions of the model.

Interaction	Predicted Polarization	Incident Beam Polarization	Predicted Value
$n \to \Xi^-$	$\frac{-1.6d-10.8\epsilon}{8d\epsilon+10.8}$	$d = -\frac{40}{42}\epsilon \approx -\epsilon$	$-0.079 - -0.091$
$\Lambda^0 \to \Xi^-$	$\frac{d-0.6\epsilon}{2d\epsilon+6.8}$	$d = -\epsilon$	$-0.022 - -0.026$
$\Xi^0 \to \Xi^-$	$\frac{2d+3.8\epsilon}{4d\epsilon+4.6}$	$d = -\epsilon$	$+0.033 - +0.045$
$n \to \Omega^-$	0	0	0
$\Lambda^0 \to \Omega^-$	$\frac{5}{6}\frac{0.8d+1.2(\epsilon-\delta)}{1.2}$	$d = -\epsilon$	$-0.047 - -0.055$
$\Xi^0 \to \Omega^-$	$\frac{10(d-\epsilon+\delta)+0.8(5\delta-6\epsilon)}{2d(5\delta-4\epsilon)+17.6}$	$d = -\epsilon$	$-0.054 - -0.069$

Table 6.2: Predicted polarizations for production from a polarized neutral beam. The range of predicted values show the effect of a $\pm$ 10% difference between the values of δ and ϵ.

The predictions of this model for a polarized incident beam are given in Table 6.2. The range of predicted values show the effect of a $\pm$ 10% difference in the values of δ and ϵ. The effect of neglecting the spin flip contributions is to increase the magnitude of the predicted Ω^- polarizations by 2% - 3%. The values used for the incident beam polarization are based on the DeGrand and Miettinen model predictions for the production of the neutral beam components from protons.

For the Ξ^-, the largest predicted polarization is for production from neutrons, however, this interaction is not expected to contribute much to the final sample. The predictions for Λ^0 and Ξ^0 production have opposite signs, but similar magnitudes. The prediction for Λ^0 production, which is thought to be the dominant production mode, does have the same sign as the observed polarization, however, both of these predictions are much smaller in magnitude than the observed polarization of -0.118 ± 0.008.

For the Ω^-s, no polarization is predicted for production from neutrons. The predicted polarization for Λ^0 and Ξ^0 production are similar in sign and magnitude (-0.05 to -0.07), and both predictions are consistent with the observed value of -0.069 ± 0.023.

Of the four cases studied in this experiment (production of Ξ^-s and Ω^-s from polarized and unpolarized neutral beams), the model of DeGrand and Miettinen is successful only in the case of Ω^- production by a polarized neutral beam. For Ξ^- production from a polarized neutral beam and Ω^- production from an unpolarized neutral beam, the magnitudes of the observed polarizations are larger than the predictions. For Ξ^- production from an unpolarized neutral beam, no polarization is observed. In this case, the dominant contribution is thought to be Λ^0 production, which is predicted to be small. However, the polarization prediction for Ξ^0 production is large, so evaluating the success of the DeGrand and Miettinen model in this case is difficult.

6.2.1 Other possible explanations

In the DeGrand and Miettinen model, all of the quarks are treated in the same manner. However, it is certainly plausible to expect that the polarization of the quarks produced from the sea depends on the type of quark produced since the s quark is heavier than the u and d quarks. It is interesting to note that all of the Ω^- production reactions have a change in strangeness between the initial and final states, and that we observe polarization in our sample of Ω^- produced from the unpolarized neutral beam. However, for the Ξ^-s, production from a Ξ^0 is a $\Delta S = 0$ interaction, and no polarization is observed in the unpolarized neutral beam production mode.

Results from a recent experiment could also support this idea [53]. In this experiment, a beam of Σ^- hyperons was used to produce a sample of Λ^0s, $\overline{\Lambda}^0$s, Σ^+s, and Ξ^-s. The polarization of the Ξ^-s was found to be similar in both magnitude and sign to samples of Λ^0s produced from protons. However, the polarization of the Λ^0s and Σ^+s was found to be small or zero, but definitely not as large as the polarization of the Ξ^-s. The Λ^0 and Σ^+ production process had no change in strangeness, whereas Ξ^- production did involve a change in the number of strange quarks.

All of the quark level models that attempt to explain the polarization phenomena are based on the simple baryon wave-functions given in Table 1.1. It is possible that the actual baryon wave functions are more complicated. If, in addition to spin angular momentum, the ground state baryon wave functions also contained orbital angular momentum, then a possible explanation of the observed polarizations is that the production process favors certain orbital angular momentum configurations. Then, since the final state must have a total spin of $\frac{1}{2}$ (or $\frac{3}{2}$ for the Ω^-), there could be a preferred spin orientation for the quark or quarks from the sea that combine with the incident fragment to produce the observed final state.

6.3 Summary

To summarize, the polarization of Ξ^-s and Ω^- produced by an unpolarized neutral beam has been has been measured for the first time. The Ξ^-s were found to be unpolarized. The observed Ω^- polarization was $+0.044\pm0.008$ at an average momentum of 394. GeV/c and $+0.036\pm0.015$ at an average momentum of 305. GeV/c. These values are smaller than the theoretical predictions. The sign of this observed Ω^- polarization is also opposite that predicted by one theoretical model. This rules out the picture that hyperon polarization is due to the conservation of angular momentum during the production of quark – anti-quark pairs from the sea.

The polarization of Ξ^-s and Ω^-s produced by a polarized neutral beam was also studied. The Ξ^- sample had a polarization of -0.118 ± 0.004 at an average momentum of 393. GeV/c. The Ω^- sample had a polarization of -0.069 ± 0.023 at an average momentum of 394. GeV/c. Both of these results agree with a previous measurement. The observed polarization of both particles have larger magnitudes than theoretical predictions.

None of the current models that attempt to explain the phenomena of hyperon

polarization gives a satisfactory explanation of these results. The results for production from an unpolarized neutral beam could indicate that polarization may only appear in interactions where there is a change in strangeness between the initial and final state. These results would also not rule out the idea that the ground state baryon wave functions involve orbital angular momentum components in addition to spin angular momentum components.

This experiment has studied the polarization of hyperons produced from an unpolarized beam of neutral particles. This is one of the first instances where the polarization of hyperons produced from baryons other than protons has been studied. The results of this experiment have pointed out problems with two theoretical models, and it is hoped that these results will offer further insight into the origin of hyperon polarization.
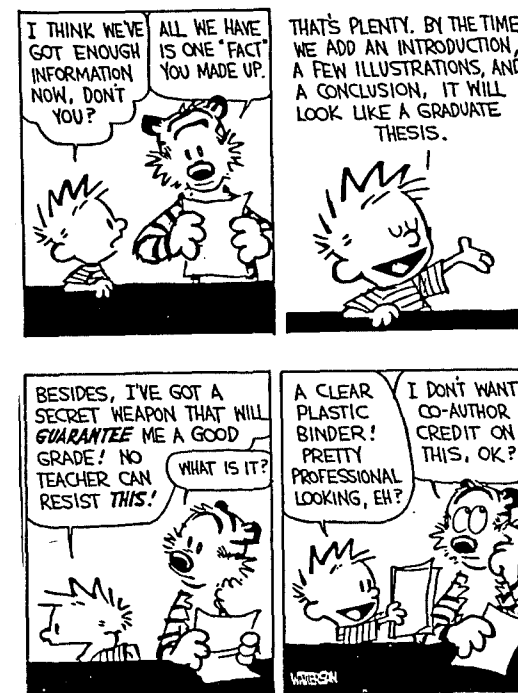
CALVIN AND HOBBES copyright Watterson. Dist. by UNIVERSAL PRESS SYNDICATE. Reprinted with permission. All rights reserved.

Appendix A

Calculation of Polarization

prediction for $\Xi^0 \to \Xi^-$

This appendix shows a sample calculation of a polarization prediction including the allowance for a spin flip before the recombination into the final state.

First, we start by writing the wave functions for the Ξ^0 and Ξ^- for both the spin up and spin down states. They are as follows:

$$\Xi^0 \uparrow \ : \ \sqrt{\frac{2}{3}} u \downarrow ss_{11} - \sqrt{\frac{1}{3}} u \uparrow ss_{10} \tag{A.1}$$

$$\Xi^0 \downarrow \ : \ \sqrt{\frac{1}{3}} u \downarrow ss_{10} - \sqrt{\frac{2}{3}} u \uparrow ss_{1-1} \tag{A.2}$$

$$\Xi^- \uparrow \ : \ \sqrt{\frac{2}{3}} d \downarrow ss_{11} - \sqrt{\frac{1}{3}} d \uparrow ss_{10} \tag{A.3}$$

$$\Xi^- \downarrow \ : \ \sqrt{\frac{1}{3}} d \downarrow ss_{10} - \sqrt{\frac{2}{3}} d \uparrow ss_{1-1} \tag{A.4}$$

where ss_{nm} is a shorthand for a pair of s quarks in a spin state with total spin n and spin z-component m. In the notation of DeGrand and Miettinen, this is a VVS process, meaning that the final state contains two valence quarks from the incident particle, two s quarks in this case, and one quark from the sea, a d quark here [30]. The first step, is to calculate the matrix element for each of the four possible interactions. They are

as follows:

$$\langle \Xi^- \uparrow |T| \Xi^0 \uparrow \rangle \ = \ \frac{2}{3} B_\downarrow A_{11} + \frac{1}{3} B_\uparrow A_{10} \tag{A.5}$$

$$\langle \Xi^- \uparrow |T| \Xi^0 \downarrow \rangle \ = \ -\frac{1}{3} B_\uparrow A_{10} \tag{A.6}$$

$$\langle \Xi^- \downarrow |T| \Xi^0 \uparrow \rangle \ = \ -\frac{1}{3} B_\downarrow A_{10} \tag{A.7}$$

$$\langle \Xi^- \downarrow |T| \Xi^0 \downarrow \rangle \ = \ \frac{1}{3} B_\downarrow A_{10} + \frac{2}{3} B_\uparrow A_{1-1} \tag{A.8}$$

where $B_\uparrow$ and $B_\downarrow$ are the amplitudes due to spin up and spin down sea quarks, and A_{nm} is the amplitude due to a valence quark pair in a state ss_{nm}. Next, we calculate the cross sections by taking the squares of these amplitudes, neglecting any incoherent cross-terms, and using the following parameterization of the valence and sea quark amplitudes:

$$|B_\uparrow|^2 \ = \ B(1 - \epsilon) \tag{A.9}$$

$$|B_\downarrow|^2 \ = \ B(1 + \epsilon) \tag{A.10}$$

$$|A_{1m}|^2 \ = \ A(1 + m\delta) \tag{A.11}$$

$$|A_{00}|^2 \ = \ A \tag{A.12}$$

With this parameterization, the cross sections, $w_{b'b}$, where b is the spin of the produced particle and b' is the spin of the incident particle, are written as:

$$w_{\frac{1}{2}\frac{1}{2}} \ = \ \frac{AB}{9}(5 + 4\delta + 3\epsilon) \tag{A.13}$$

$$w_{\frac{1}{2}-\frac{1}{2}} \ = \ \frac{AB}{9}(1 - \epsilon) \tag{A.14}$$

$$w_{-\frac{1}{2}\frac{1}{2}} \ = \ \frac{AB}{9}(1 + \epsilon) \tag{A.15}$$

$$w_{-\frac{1}{2}-\frac{1}{2}} \ = \ \frac{AB}{9}(5 - 4\delta - 3\epsilon) \tag{A.16}$$

Now, we can calculate $\mathcal{A}$, the asymmetry of this interaction. The asymmetry is the difference between the probability for a spin up final state minus the probability for a

spin down final state over the total probability, and can be written as:

$$\mathcal{A} = \frac{\sum_{b'} \frac{1}{2}(w_{\frac{1}{2}b'} - w_{-\frac{1}{2}b'})}{\sum_{bb'} |b| w_{bb'}} \tag{A.17}$$

Doing this for the case with no polarization of the incident beam, we find:

$$\mathcal{A} = \frac{\epsilon + 2\delta}{3} \tag{A.18}$$

If this incident beam is polarized, with x particles with spin up, and $(1-x)$ particles spin down, the cross sections calculated above need to be weighted accordingly. If this is done, the prediction for the asymmetry becomes:

$$\mathcal{A} = \frac{2d + \epsilon + 2\delta}{2d(\delta + \epsilon) + 3} \tag{A.19}$$

where $d = 2x - 1$ is the polarization if the incident beam.

This model has been extended by allowing for the possibility that the quark pair from the incident particle will undergo a spin flip before combining with the quark from the sea [21]. Allowing for this, the matrix elements calculated above become:

$$\langle \Xi^- \uparrow |T| \Xi^0 \uparrow \rangle = \frac{2}{3}B_\downarrow A_{11} + \frac{1}{3}B_\uparrow A_{10} - \frac{\sqrt{2}}{3}B_\uparrow A_{10}^\tau - \frac{\sqrt{2}}{3}B_\downarrow A_{11}^\tau \tag{A.20}$$

$$\langle \Xi^- \uparrow |T| \Xi^0 \downarrow \rangle = -\frac{1}{3}B_\uparrow A_{10} + \frac{\sqrt{2}}{3}B_\downarrow A_{11}^\tau + \frac{\sqrt{2}}{3}B_\uparrow A_{10}^\tau \tag{A.21}$$

$$\langle \Xi^- \downarrow |T| \Xi^0 \uparrow \rangle = -\frac{1}{3}B_\downarrow A_{10} + \frac{\sqrt{2}}{3}B_\downarrow A_{10}^\tau + \frac{\sqrt{2}}{3}B_\uparrow A_{1-1}^\tau \tag{A.22}$$

$$\langle \Xi^- \downarrow |T| \Xi^0 \downarrow \rangle = \frac{1}{3}B_\downarrow A_{10} + \frac{2}{3}B_\uparrow A_{1-1} - \frac{\sqrt{2}}{3}B_\uparrow A_{1-1}^\tau - \frac{\sqrt{2}}{3}B_\downarrow A_{10}^\tau \tag{A.23}$$

where A_{nm}^τ is the amplitude due to a valence quark pair that has undergone a spin flip into a ss_{nm} state.

With these new matrix elements, the cross sections are:

$$w_{\frac{1}{2}\frac{1}{2}} = \frac{AB}{9}(5 + 4\delta + 3\epsilon) + \frac{AB}{9}\tau_2(4 + 2\delta) \tag{A.24}$$

$$w_{\frac{1}{2}-\frac{1}{2}} = \frac{AB}{9}(1 - \epsilon) + \frac{AB}{9}\tau_2(4 + 2\delta) \tag{A.25}$$

$$w_{-\frac{1}{2}\frac{1}{2}} = \frac{AB}{9}(1 + \epsilon) + \frac{AB}{9}\tau_2(4 - 2\delta) \tag{A.26}$$

$$w_{-\frac{1}{2}-\frac{1}{2}} = \frac{AB}{9}(5 - 4\delta - 3\epsilon) + \frac{AB}{9}\tau_2(4 - 2\delta) \tag{A.27}$$

where the parameterization $|A_{mn}^\tau|^2 = \tau_2 A(1 + m\delta)$ has been used. Here, τ_2 is determined from the probability $\mathcal{P}$ of a single spin flip.

$$\tau_2 = \frac{2\mathcal{P}(1 - \mathcal{P})}{1 - 2\mathcal{P}(1 - \mathcal{P})} \tag{A.28}$$

With these cross sections, the asymmetry can be calculated. Allowing for a polarized incident beam, the asymmetry is:

$$\mathcal{A} = \frac{2d + \epsilon + 2\delta(1 + \tau_2)}{2d(\delta + \epsilon) + 3 + 4\tau_2} \tag{A.29}$$

As a consistency check, we see that if we set $\tau_2 = 0$, we get the expression in Equation A.19, and if we set $\tau_2 = 0$ and $d = 0$, we get the result expressed in Equation A.18.

Chamber	view	Particle	Proton	π	π/K_s
C6	x	Ξ^-	X	X	X
		Ω^-	X	X	X
	y	Ξ^-	X	X	X
		Ω^-			
C9	x	Ξ^-	X	X	X
		Ω^-	X	X	
	y	Ξ^-	X	X	X
		Ω^-			
C10	x	Ξ^-		X	
		Ω^-			
	y	Ξ^-	X	X	X
		Ω^-	X	X	X

Table B.1: Summary of hits required in the hybrid Monte Carlo polarization analysis.

Chamber	view	particle	$P-\pi$	$\pi-\pi/K_s$	$P-\pi/K_s$
C6	x	Ξ^-	3	2	2
		Ω^-	2	1	1
	y	Ξ^-	2	3	4
		Ω^-	1	1	1
C9	x	Ξ^-	4	2	2
		Ω^-	3	1	1
	y	Ξ^-	3	2	3
		Ω^-	3	1	3
C10	x	Ξ^-	1	3	1
		Ω^-	1	1	1
	y	Ξ^-	1	1	3
		Ω^-	1	1	1
C11	x	Ξ^-	0	0	0
		Ω^-	0	0	0
	y	Ξ^-	1	1	1
		Ω^-	1	1	1

Table B.2: Summary of track separations required in the hybrid Monte Carlo polarization analysis. The separations are expressed in terms chamber wire spacings, which is 2mm for all the chambers listed in the table.

Appendix B

Hybrid Monte Carlo Topological

Selection Criteria

A number of topological selection criteria were imposed on the real and fake events used in the hybrid monte carlo polarization analysis. Some of these selection criteria were dictated by the spectrometer. Any fake event wire hits in the MWPCs that fell outside the active region of a chamber were neglected. The fake events had to satisfy the $(C11)_\pi \cdot (C12)_{proton}$ part of the trigger.

Additional requirements involving the hits used on the various particle tracks and the separation of these track were imposed. Different criteria were used on the Ω^- and Ξ^- samples. The small size of the Ω^- sample dictated that the required hit and track separation requirements not reduce that sample size significantly, whereas the large Ξ^- sample allowed more extensive cuts. The required hits are listed in Table B.1. These requirements were developed through extensive systematic studies. Similar systematic studies were performed to test the track separation cuts listed in Table B.2. The main purpose of these selection criteria was to correct for the known limitations of the reconstruction process.

References

[1] R. M. Woods and B. J. Spence, Phys. Rev. 4, 669, (1934).

[2] R. M. Woods, Jr., Ph.D. Thesis, "Improvements in Beta Spectroscopy and the Decay of Samarium-153, Dysprosium-165, and Cesium-134", University of Michigan, (1963), unpublished.

[3] G. Bunce et al., Phys. Rev. Lett. 36, 1113, (1976).

[4] R. O. Polvado et al., Phys. Rev. Lett. 42, 1325, (1979).

[5] K. Heller et al., Phys. Rev. Lett. 41, 607, (1978).

[6] C. Ankenbrandt et al., Phys. Rev. Lett. 51, 863, (1983).

[7] L. Deck et al., Phys. Rev. D 28, 1, (1983).

[8] C. Dukes et al., Phys. Lett. 193B, 135, (1987).

[9] A. Morelos et al., Phys. Rev. Lett. 71, 2172, (1993).

[10] R. Rameika et al., Phys. Rev. D 33, 3172, (1986).

[11] K. Heller et al., Phys. Rev. Lett. 51, 2025, (1983).

[12] P. M. Ho et al., Phys. Rev. Lett. 65, 1713, (1990).

[13] K. B. Luk et al., Phys. Rev. Lett. 70, 900, (1993).

[14] J. Bensinger et al., Phys. Rev. Lett. 50, 313, (1983).

[15] B. Edelman et al., Phys. Rev. Lett. 40, 491, (1978).

[16] S. U. Chung et al., Phys. Rev. D 11, 1010, (1975).

[17] G. T. Jones et al., Z. Phys. C 28, 23, (1985).

[18] K. Abe et al., Phys. Rev. D 29, 1877, (1984).

[19] B. E. Bonner et al., Phys. Rev. Lett. 58, 447, (1987).

[20] B. E. Bonner et al., Phys. Rev. D 38, 729, (1988).

[21] B. E. Bonner et al., Phys. Rev. Lett., 62, 1591, (1989).

[22] T. Henkes et al., Phys. Lett. 283B, 155, (1992).

[23] B. Lundberg et al., Phys. Rev. D 40, 3557, (1989).

[24] J. Duryea et al., Phys. Rev. Lett. 67, 1193, (1991).

[25] H. T. Diehl, Ph.D. thesis, "Omega Minus Polarization and Magnetic Moment", Rutgers University, (1990), unpublished.

[26] H. T. Diehl et al., Phys. Rev. Lett. 67, 804, (1991).

[27] G. L. Kane et al., Phys. Rev. Lett. 41, 1689, (1978).

[28] F. Halzen and A. D. Martin, "Quarks and Leptons", p. 171, John Wiley & Sons, (1984).

[29] T. A. DeGrand and H. I. Miettinen, Phys. Rev. D 24, 2419, (1981).

[30] T. A. DeGrand et al., Phys. Rev. D 32, 2445, (1985).

[31] P. Kroll, in *High Energy Spin Physics Eighth International Symposium*, edited by K. Heller, AIP Conference Proceedings No. 187 (American Institute of Physics, New York, 1989), p. 48.

[32] M. W. Sullivan *et al.*, Phys. Rev. D **36**, 674, (1987).

[33] B. Andersson, G. Gustafson, and G. Ingelman, Phys. Lett. **85B**, 417, (1979).

[34] J. Szwed, Phys. Lett. **105B**, 403, (1981).

[35] W. G. D. Dharmaratna and G. R. Goldstein, Phys. Rev. D **41**, 1731, (1990).

[36] R. Barni *et al.*, Phys. Lett. **296B**, 251, (1992).

[37] J. Soffer and N. A. Törnqvist, Phys. Rev. Lett. **68**, 907, (1992).

[38] H. Haggerty *et al.*, NIM **115**, 157, (1974).

[39] S. Hansen *et al.*, IEEE Trans. Nuc. Sci. **NS-34**, 1003, (1987).

[40] Particle Data Group, Phys. Rev. D **50**, 1173, (1994).

[41] T. D. Lee *et al.*, Phys. Rev. **106**, 1367, (1957).

[42] T. D. Lee and C. N. Yang, Phys. Rev. **108**, 1645, (1957).

[43] O. E. Overseth and S. Pakvasa, Phys. Rev. **184**, 1663, (1969).

[44] M. Deutschmann *et al.*, Phys. Lett. **73B**, 98, (1978).

[45] M. Baubillier *et al.*, Phys. Lett. **78B**, 342, (1978).

[46] K. B. Luk *et al.*, Phys. Rev. D **38**, 19, (1988).

[47] G. M. Guglielmo, Ph. D. thesis, "Measurement of the Decay Asymmetries of the Omega-Minus Baryon", University of Minnesota, (1994), unpublished.

[48] J. Finjord, Phys. Lett. **76B**, 116, (1978).

[49] J. Finjord and M. K. Gaillard, Phys. Rev. D **22**, 778, (1980).

[50] H. Galic, D. Tadic, and J. Trampetic, Phys. Lett. **89B**, 249, (1980).

[51] G. Bunce, NIM **172**, 553, (1980).

[52] N. B. Wallace, Ph. D. thesis, "A Precision Measurement of the Magnetic Moment of the Omega Minus Hyperon", University of Minnesota, (1995), unpublished.

[53] M. I. Adamovich *et al.*, CERN-PPE/94-86, (1994).